In vitro and in vivo study on fine-grained Mg–Zn–RE–Zr alloy as a biodegradeable orthopedic implant produced by friction stir processing

Vasanth C. Shunmugasamy [a], Marwa AbdelGawad [a,b], Muhammad Umar Sohail [c], Talal Ibrahim [d,e], Talha Khan [f], Thomas Daniel Seers [f], Bilal Mansoor [a,b,g,*]

[a] Mechanical Engineering Program, Texas A&M University at Qatar, Education City, Doha, Qatar
[b] Department of Mechanical Engineering, Texas A&M University, 3123 TAMU, College Station, TX 77843, USA
[c] Proteomics Core, Weill Cornell Medicine, Education City, Doha, Qatar
[d] Department of Surgery, Division of Orthopedic Surgery, Sidra Medicine, Doha, Qatar
[e] Clinical Orthopedic Surgery, Weill Cornell Medicine, Education City, Doha, Qatar
[f] Petroleum Engineering Program, Texas A&M University at Qatar, Education City, Doha, Qatar
[g] Department of Materials Science and Engineering, Texas A&M University, 3003 TAMU, College Station, TX 77843, USA

ARTICLE INFO

ABSTRACT

Magnesium alloys containing biocompatible components show tremendous promise for applications as temporary biomedical devices. However, to ensure their safe use as biodegradeable implants, it is essential to control their corrosion rates. In concentrated Mg alloys, a microgalvanic coupling between the α-Mg matrix and secondary precipitates exists which results in increased corrosion rate. To address this challenge, we engineered the microstructure of a biodegradable Mg–Zn–RE–Zr alloy by friction stir processing (FSP), improving its corrosion resistance and mechanical properties simultaneously. The FS processed alloy with refined grains and broken and uniformly distributed secondary precipitates showed a relatively uniform corrosion morphology accompanied with the formation of a stable passive layer on the alloy surface. In vivo corrosion evaluation of the processed alloy in a small animal model showed that the material was well-tolerated with no signs of inflammation or harmful by-products. Remarkably, the processed alloy supported bone until it healed till eight weeks with a low in vivo corrosion rate of 0.7 mm/year. Moreover, we analyzed blood and histology of the critical organs such as liver and kidney, which showed normal functionality and consistent ion and enzyme levels, throughout the 12-week study period. These results demonstrate that the processed Mg–Zn–RE–Zr alloy offers promising potential for osseointegration in bone tissue healing while also exhibiting controlled biodegradability due to its engineered microstructure. The results from the present study will have profound benefit for bone fracture management, particularly in pediatric and elderly patients.

1. Introduction

Bone fracture management involves fixation using an implant to support bone/tissue healing followed by its removal [1,2]. Permanent implants made from titanium, stainless steel and cobalt-chromium have been commonly used in orthopedic surgeries [3]. Patients can benefit from biodegradable implants by avoiding secondary removal surgery, reducing pain, physical discomfort, and cost savings [4,5]. Essential requirements for biodegradable bone implant material include biocompatibility with living tissues, mechanical integrity over its intended service life and controlled degradation coupled with non-toxic

byproducts [5]. Amongst different biodegradable metals, Mg alloys have been found to possess optimal mechanical properties that are closet to bones and good biocompatibility [6–8]. Consequently, Mg based alloys have been extensively researched for biodegradable implant application [6–14].

Mg alloys utilization as implants is impeded by their comparatively high corrosion rates. Mg has a low electrode potential of −2.372 V [15] against normal hydrogen electrode, making it extremely active in aqueous media containing chloride ions, such as human body physiological conditions. Although $Mg(OH)_2$ formed during exposure to aqueous media can act as a passive surface film [16,17], Mg exhibits

---

negative difference effect, whereby both hydrogen evolution and corrosion rate of magnesium grows with increasing potential [18,19], leading to unstable passive film. Rapid corrosion can cause the implant to lose its mechanical integrity before bone healing and promote hydrogen gas accumulation leading to subcutaneous swelling [10,20].

Ideally, Mg alloy biodegradable implants should be able to mechanically support bone during healing, commensurately degrading as healing completes. Many studies on biodegradable orthopedic implants have suggested bone tissue healing varies between 3 and 12 months [8, 10,21,22], based upon works of Erinc et al. [23], and Erbel et al. (clinical trials of cardiovascular Mg scaffolds) [24]. Therefore, the implant is expected to completely degrade within a period of 12–24 months [25, 26]. Based on this proposed bone healing period, a preferred corrosion rate of <0.5 mm/year for biodegradable Mg implants has been suggested [8,10]. However, it has been shown that several factors such as type of bone tissue, fracture location, and patient age significantly affect healing times [27–29]. Hence design criteria for biodegradable Mg alloys should be based on tissue specific corrosion rates, good mechanical properties, and alloy constituents with null toxic side effects.

To achieve an optimal biodegradable Mg based alloy, several techniques have been proposed, such as alloying additions, grain refinement and coatings to improve its mechanical and corrosion properties [8]. Among the different Mg alloying additions, Zn, Zr and RE have been shown to influence both mechanical and corrosion properties [8,16,30]. Mg–Zn and Mg-RE alloys presents one of the most favorable mechanical properties (strength and ductility) [8,31,32]. Addition of 3 wt% of Zn (a trace nutrient element [8,33]), has shown optimal increase in Mg alloy

mechanical and corrosion resistance [34–36] and hence used in present study. Zr is a grain refiner and microstructure stabilizer for Mg alloys [37–39] and its addition to Mg–Zn alloy system has shown 57% and 10% increase in yield and tensile strength, respectively [40]. Although there have been apprehensions about alloying Mg with RE [41,42], it has been suggested that the quantity of RE in Mg alloys should be optimized to prevent toxicity whilst improving alloy mechanical properties [43]. Long term in vivo studies of Mg-RE biodegradable alloys, did not reveal statistically significant accumulations of RE in critical organs or immediate bone surrounding [44,45]. These results showed that, ostensibly, RE additions in Mg alloys may not lead to adverse effects within subjects, and it was metabolized, leading to homeostatic levels being achieved.

Considering characteristics of different alloying elements, we narrowed down to Mg–Zn–RE–Zr alloy (ZE and EZ series) for biodegradable implant application, owing to their favorable mechanical and corrosion properties. The microstructure of this alloy system comprises α-Mg with T-phase secondary precipitates along grain boundaries and Zr-rich phase in grain interior (Fig. 1(b)). In our previous work, on mechanical and corrosion properties of EZ33 and ZE41 alloys, it was observed that EZ33 had lower mechanical properties compared to ZE41, but relatively more uniform corrosion properties [46–48]. The observed corrosion resistance in EZ33 alloy was attributed to development of a more stable protective surface film, evidenced by higher open circuit potential (OCP) for the alloy [46,47]. Both the T-phase and Zr-rich precipitate act as cathode to the anodic α-Mg matrix in Mg–Zn–Zr-RE alloys [49]. In EZ33 Mg alloy, micro galvanic coupling occurred between the T-phase
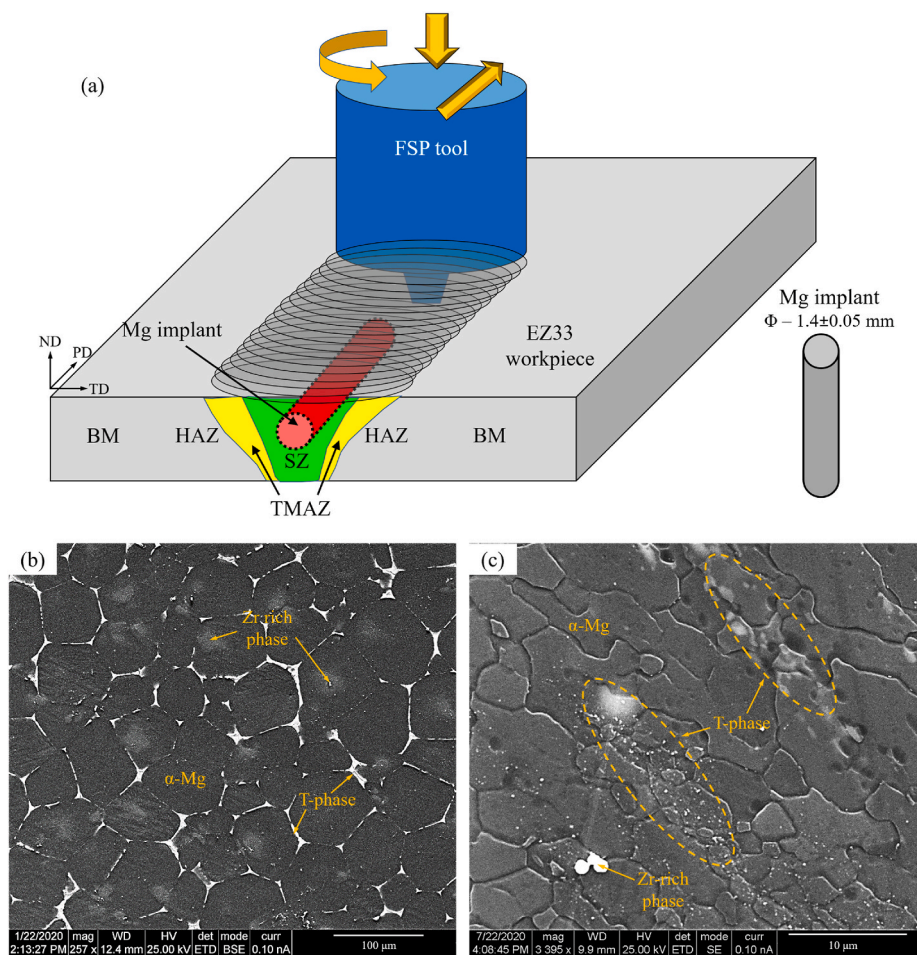

Fig. 1. (a) Schematic of friction stir processing of EZ33 Mg plate and retrieval of Mg implant from the stir zone. (b) Microstructure of EZ33 base material shows T-phase precipitates along grain boundaries and Zr rich phase in the middle of α-Mg grains. (c) Friction stir processed EZ33 size zone shows refined grains and broken-down T-phase precipitates, compared to base material.

precipitate and matrix leading to loss of precipitates, however the Zr-rich region did not influence the alloy corrosion response [48]. Consequently, EZ33 alloy showed more uniform corrosion and higher corrosion resistance compared to ZE41 alloy, resulting in better mechanical integrity [48].

To achieve relatively uniform corrosion on the selected Mg alloy, secondary precipitates must be distributed uniformly along with refined grains. Several severe plastic deformation (SPD) techniques have been adopted to modify Mg alloy microstructure [50,51]. Corrosion in Mg is high, due to poor stability of the passive oxide layer caused by compression stresses therein, owing to its geometrical incompatibility with the hexagonal base Mg lattice [52]. As a result of SPD process, grain boundaries are increased which minimizes mismatch between the oxide/hydroxide layer and the base Mg substrate, leading to improved corrosion properties [52]. Friction stir processing (FSP) is a SPD process, in which a rotating tool is plunged into the workpiece and translated to modify its microstructure [53]. Mg-RE alloy subjected to FSP showed refined grains (0.7 μm from 70 μm) resulting in decreased corrosion rate (0.04 mg/cm². day from 0.18 mg/cm². day), owing to higher grain boundary per unit volume, leading to improved passivation kinetics [54]. Mg–Zn-RE alloy processed using FSP showed decreased secondary phases volume fraction, compared to base material [55]. Refined grains and lower secondary phases resulted in higher corrosion resistance, due to more uniform corrosion behavior and re-dissolution of secondary phases into the matrix [55].

Texture is another critical factor influencing corrosion response of Mg alloys. Studies have shown that for Mg alloys, basal texture, shows improved corrosion resistance than non-basal textures [56–60]. Studies on AZ31 alloy exposed to corrosion medium, observed that grains with non-basal planes suffered greater corrosion attack in comparison to grains with basal planes [57,61]. Similar observations have been made for extruded Mg–Zn-Gd-Zr alloy where basal texture dominated extrusion surface showed higher corrosion resistance, compared to as-cast alloy with random texture [62]. Notably, Mg alloys subjected to FSP tend to exhibit dominant basal texture in the stir zone region [63–65].

Mg alloys processed through FSP has also shown considerable improvement to mechanical properties such as strength and ductility [66–68]. Magnesium has a hcp crystal structure with a limited number of independent slip systems, resulting in low room temperature ductility and formability [69]. Mechanical properties of Mg alloys are influenced by several microstructural features such as grain size, precipitates and texture [70,71]. By engineering Mg alloys microstructure, its mechanical and corrosion properties can be tailored. In the present work, the microstructure of selected EZ33 alloy is engineered using FSP as an SPD tool, with an aim to achieve the following material characteristics: (i) grain refinement to aid passivation kinetics and improve mechanical properties, (ii) reduce size and uniform distribution of secondary phases in order to reduce microgalvanic effects and (iii) develop a favorable texture. The processed Mg alloys are subjected to in vitro and in vivo characterization to study corrosion response. The in vivo section has been designed such that the corrosion rate of processed Mg alloy implant, can be directly compared with bone tissue healing. The study aims to address the following key questions:

- Effect of alloying elements (material selection) on in vitro and in vivo corrosion and comparison with existing alloys?
- Effect of grain size, distribution of secondary phases and texture (achieved through SPD) on in vitro and in vivo corrosion of selected alloy?
- To what extent is the animal model able to remodel the fracture around the implant (osseointegration) and other effects on critical organs functioning?
- How close is the match between corrosion of microstructure engineered biodegradable Mg alloy implant compared with real time healing of bone tissue?

2. Materials and methods

2.1. Severe plastically deformed EZ33 implant material

In the present work, EZ33A Mg alloy in T5 condition is utilized as the implant base material (BM). Chemical composition and microstructure of BM are shown in Table 1 and Fig. 1 respectively. To refine the grains of EZ33 BM, friction stir process, a severe plastic deformation methodology was employed. FSP was carried out on a 3 mm thick EZ33-BM plate using an FSP machine (CFSWT, Beijing) containing a tool with a shoulder diameter of 12 mm, and with a 2.8 mm long conical pin (5 mm major diameter and 3 mm minor diameter) (Fig. 1(a)). The processing (PD), normal (ND) and transverse (TD) directions with respect to the workpiece is shown in Fig. 1(a). Process parameters utilized include a tool rotational speed of 1500 rpm, translation speed of 20 mm/min and tool tilt angle of 2°. The resulting microstructure from FSP contained the stir zone (SZ), thermomechanical affected zone (TMAZ), heat affected zone (HAZ) and base material (BM) (Fig. 1(a)). Since the stir zone undergoes severe plastic deformation and results in refined grains as shown in Fig. 1(c), the implant to be used for in vitro and in vivo testing was cut from the stir zone with diameter of 1.4 ± 0.05 mm using an electric discharge machine. To assess the impact of subjecting the Mg alloy material through FSP using a steel tool, the processed region (3 g specimen) was analyzed for chemical composition variation pre- and post-processing using inductively coupled plasma (ICP) analysis (IMR Test Labs, NY).

2.2. Microstructural and texture characterization

Microstructural examination of the base material and FSP samples was carried out on sample cuts from the top surface (normal plane) and cross-section (processing plane) of the SZ. Samples were epoxy mounted, grinded and polished up to 1 μm, using diamond suspensions. To reveal the microstructure, samples were etched with acetic picral solution [72]. A FEI Quanta 400 scanning electron microscope (SEM) with backscatter electron (BSE) imaging and Energy Dispersive X-ray spectroscopy (EDS) operated at 20 keV was used to examine secondary phases, chemical composition, surface morphology of post-immersion corroded samples. Grain size was measured by averaging more than 50 grain size diameters from 5 different microstructures for statistical relevance. X-Ray Diffraction (XRD) was performed on the EZ33-BM specimen to identify its constituent phases. Texture analysis was performed using FEI field emission scanning microscope fitted with electron backscatter diffraction (EBSD) analyzer, using 20 keV accelerating voltage, 10 nA probe current and confidence index of 0.1. The pole figures were obtained using the EBSD orientation imaging data.

2.3. Mechanical property evaluation

The EZ33 alloy specimens were evaluated for Vickers microhardness (Future Tech FM-310, Japan) using 100 gf load and a dwell time of 15 s. The tensile test was conducted using electromechanical MTS Insight 30 kN load tensile tester at ambient temperature with an initial strain rate of 10^{-3}/s. Tensile specimen had nominal cross-sectional area of 3×3 mm² and a gauge length of 12 mm.

2.4. In vitro corrosion

Immersion test, using the weight loss method, was implemented to assess the in vitro degradation behavior of the implants. Samples similar in dimension to those used for in vivo testing, were immersed in 250 ml Hank's balanced salt solution (HBSS, Sigma Aldrich) at 37 ± 1 °C, to simulate body conditions. Samples were removed at different time intervals, washed with distilled water, air-dried and weighed. The calculated corrosion in mm/yr is given by Ref. [73]:

Table 1
Chemical composition of EZ33A Mg alloy utilized in present work [47].

Element	Zn	Zr	Ce	La	Nd	Mn	Fe	Cr	Mg
Wt.%	2.66	1.32	1.16	0.47	0.26	0.01	<0.01	<0.01	Balance

$$\text{Corrosion rate} = \left(\frac{8760 \times \text{mass loss (g)}}{\text{Exposed area (mm}^2) \times \text{time (h)} \times \text{density (g/mm}^3)} \right) \quad (1)$$

From the initiation of immersion, weight measurements were taken at hourly intervals in order to capture the initial rapid corrosion response. Later, the interval between measurements was increased and samples were immersed for a total duration of 12 weeks. In-situ corrosion tests (i.e. drop tests), were carried out by wetting the polished surface of the base and processed material with HBSS and monitored using an optical microscope. The drop test aided observation of the corrosion front's evolution and propagation, as well as the occurrence of micro-galvanic effects in real time.

Electrochemical measurements were conducted at $37 \pm 1 \,^\circ\text{C}$ in HBSS for a period of 24 h on specimen with 1 cm^2 cross sectional area in 250 ml solution. The pH was maintained at 7.4 ± 0.1 using HEPES (4-(2-hydroxyethyl)-1-piperazineethanesulfonic acid) buffering solution to provide a more realistic representation of the corrosion process as it would occur within the human body. Open circuit potential (OCP), potentiodymamic polarization (PDP), and electrochemical impedance spectroscopy (EIS) techniques were used to study corrosion behavior of the base material and processed samples. A typical three-electrode setup using Gamry Eurocell™ was used, with an exposed area of 0.25 cm^2 as the working electrode, a graphite rod as counter electrode and saturated silver/silver chloride (Ag/AgCl) reference electrode. Samples were prepared using the same procedure for microstructural investigations and were immersed for 10 min to achieve constant potential before conducting the experiments. OCP was measured at different time intervals to map its variation with time, with each sampling point obtained by taking the average of the OCPs over a 30 min period. EIS measurements were taken at OCP by sweeping the frequencies from 10^5 to 10^{-2} Hz with an applied sinusoidal potential of 10 mV in amplitude. PDP scans were obtained by continuous scanning from -2.5 V vs. E_{OCP} to 1.5 V vs. E_{OCP} at a rate of 1 mV/s. Immersion and electrochemical tests were duplicated to validate the repeatability of the results.

2.4.1. Cytotoxicity

NIH3T3, mouse embryonic fibroblast cells, were cultured in Dulbecco's Modified Eagle's Medium (DMEM) supplemented with 10% fetal bovine serum (FBS), 100 U/ml penicillin, and 100 μg/ml streptomycin at 37 °C in a humidified atmosphere of 5% CO$_2$. Cytotoxicity tests of EZ33 and its major rare earth alloying elements (Nd, La and Ce) were carried out using indirect MTT (methylthiazolyldiphenyl-tetrazolium bromide) assay based on the ISO-10993-5 standards [74].

Extracts were prepared using 10 mg powdered samples and incubated in 10 ml of DMEM extraction medium with no serum addition. After eight days of incubation in humidified atmosphere at 37 °C, the NIH3T3 cells were seeded onto 96-well cell culture plates with 100 μl of medium per well and incubated for 24 h for cell attachment. The DMEM +10% FBS without metal extract was used as a negative control, while DMEM with 25% FBS and 10% DMSO (dimethyl sulfoxide) was used a positive control. 20 μl of MTT was added to each well and the samples were further incubated for 3 h at 37 °C. 100 μl of DMSO was added to each well as a stop solution and each well was incubated for 20 min before being measured spectrophotometrically at 570 nm.

Statistical analysis was performed to evaluate the difference in cell viability between the control and alloy extracts. Two-tailed *t*-test was used for three samples in each group and statistical significance was defined as $p < 0.05$.

2.5. In vivo corrosion

In vivo corrosion study was performed using 24 Sprague Dawley rats (12 male + 12 female) at the Laboratory Animal Research Center (LARC), Qatar University following IACUC protocol no: 2–6/2019-1. The male rats were 33 ± 1 weeks old with average body weight of 645 $\pm$ 43.2 g and female rats were 22 ± 1 weeks old with average body weight of 334.8 ± 28.6 g. All animals were housed in individual cages. The animals were divided in two groups: implant group (6 male + 6 females) and control group (6 males + 6 females). The implant group received our experimental alloy implant (EZ33 Mg alloy), whereas the control group underwent surgery without implant insertion. Animals were injected with a xylazine/ketamine combination (0.1 ml/100 g rat wt.) to induce anesthesia through intraperitoneal route. Fur on the hind leg was shaved to reveal skin. 5% povidone-iodine was applied as antiseptic. A scalpel with a blade (#22) was used to make an incision on the skin and muscles. Muscles were held in place with retractors to highlight the femur. Transcortically, a 1.5 mm hole was drilled into the femur with a hand drill. The implant was inserted transcortically into the femur. After the procedure the muscles and skin were approximated with absorbable and non-absorbable sutures, respectively. Meloxicam (2 mg/kg) was given to all of the animals as analgesic after surgery for three days. Post-surgery food and water were made available *ad libitum* to the animals. Three male animals (2 implant and 1 control group) of the 24 were lost within two days after the surgery. All the animals were monitored for recovery and health status. Animals were euthanized at 4, 8, and 12 weeks post surgery to investigate tissue repair, organ histology, and implant recovery. The in vivo corrosion rate (*CR*) was measured based on the implant volume loss (ΔV), exposed implant surface area (*A*) and exposure time (*t*) and was represented as [75]

$$CR = \frac{\Delta V}{A \times t} \quad (2)$$

The corrosion results were converted to median and standard deviation. Mann-Whitney *U* test was used to compare the groups at *p* value of 0.05.

2.5.1. MicroCT

The implant material was imaged using a Thermo-Fischer Heliscan (Mk1) X-ray microcomputed tomography scanner to study implant corrosion and osseointegration. Scans of animal model bones were performed using 90 kV beam voltage, 50 μA current and an 850 ms exposure time, captured using a space filling protocol. A 0.2 mm thickness stainless steel filter was placed between the source and sample to minimize beam hardening effects, with a 5 mm Al filter used at the detector. The acquired radiographs were reconstructed using iterative reconstruction, with the resultant volume images analyzed using Thermo-Fisher Avizo 9.2.0. Initially, the Non-Local Means (NLM) filter was applied to reduce image noise [76], proceeded by the application of an unsharp mask. In order to obtain image-based estimates of implant volumetric degradation, it is necessary to segment tomographic image data into its targeted component material phases (i.e. alloy implant and bone tissue). Due to similar attenuation characteristics of the studied Mg alloy implant and the surrounding bone tissue, interactive thresholding was deemed impractical. Consequently, segmentation of the implant material was carried out manually using Avizo's Segmentation Editor.

2.6. Blood serum analysis

Blood samples were taken through cardiac puncture in EDTA-coated plasma preparation tubes (Cat# 362788; BD, Mississauga, ON, Canada). Plasma samples were extracted from the blood by 30 min centrifugation at 1000*g*. The samples were preserved in duplicates at −20 °C for laboratory testing. Plasma samples were subjected to clinical chemistry measurements using a Tecan™ spectrophotometer (Infinite 200Pro, Tecan, Germany). Magnesium ions concentration was measured using colorimetric reaction in an alkaline medium that forms colored complex with xylidyl blue. The reaction between magnesium ions and reagents was observed at 520 mm wavelength and 25 °C temperature (Magnesium liquicolor, CAT# 10010, Human Diagnostica, Germany). Calcium ion concentration was estimated via a colorimetric reaction between plasma calcium ions and *o*-cresolphthalein- complex (Calcium liquicolor, CAT# 10011, Human Diagnostica, Germany). The reaction color was measured at 540 nm wavelength.

Plasma concentrations of analytes associated with kidney function were estimated using a spectrophotometer (Infinite 200Pro, Tecan, Germany). Urease enzyme converts plasma urea into ammonia and carbon dioxide. The produced ammonia reacts with hypochlorite and salicylate to form green dye (Urea liquicolor, CAT# 10505, Human Diagnostica, Germany). The color intensity was read at 540 nm wavelength. Plasma creatinine enzyme activity was measured using a multistep photometric end-point reaction. The change in color intensity was measured 10 min apart at 540 nm wavelength (Creatinine. CAT# 10053, Human Diagnostica, Germany).

Liver function test enzymes, alanine aminotransferase (ALT) and aspartate aminotransferase (ASP), and Alkaline Phosphatase (AP) enzyme activities were measured spectrophotometrically in multistep reactions. In brief, kinetic method for ALT determination used 2-oxoglutarate, NADH, and sodium azide as substrate (GPT liquiUV, CAT# 12212, Human Diagnostica, Germany). The change in color intensity was measured 10 min apart at 360 nm wavelength [77]. The ASP enzyme activity was measured using multistep reaction between 2-oxoglutarate and L-aspartate at 340 nm wavelength (GOT liquiUV, CAT# 12,211, Human Diagnostica, Germany). Alkaline Phosphatase, an important enzyme for liver function and bone development, activity was measured at 340 nm wavelength using *p*-Nitrophenyl phosphate as substrate (Alkaline Phosphatase, CAT# 12217, Human Diagnostica, Germany).

2.7. Histological specimen processing

Bone tissues collected after animal euthanasia were separated from soft tissues and fixed in 10% buffered formalin solution for histology. The bone tissues were decalcified for 48 h, with regions of interest dehydrated in ascending grades of ethanol and finally embedded in paraffin (Leica tissue embedder EG1150). Sectioning of the bone tissue was done parallel to the bone sagittal axis at thickness of 5 µm using a Leica microtome and sections were stained with Masson's trichrome stain. Liver and kidney sections were stained using Hematoxylin and
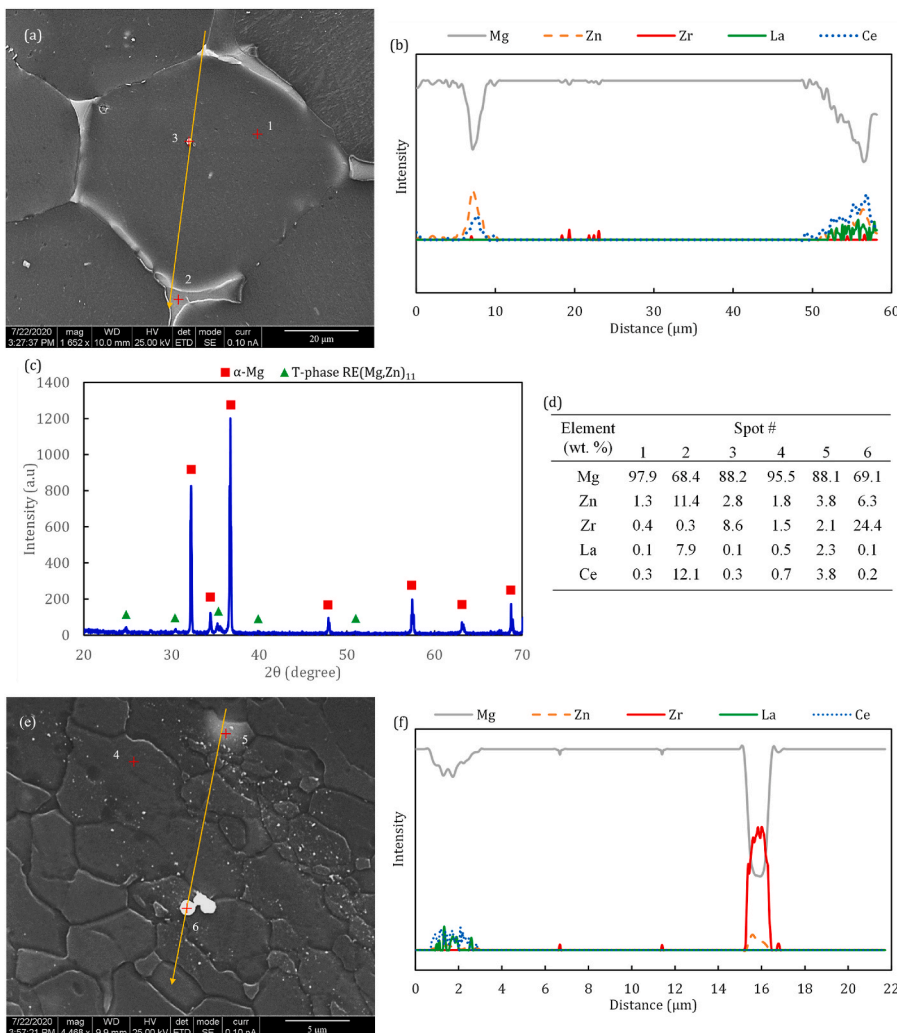

Fig. 2. (a) Microstructure of EZ33-BM showing coarse grain comprising α-Mg as matrix, T-phase as precipitates along grain boundaries and Zr-rich phase in middle of grain along with line and spot where EDS analysis was performed. (b) Variation of EDS spectra along line shown in (a) from top to bottom (c) XRD spectra of EZ33-BM. (d) Variation of elemental composition based on EDS obtained at different point on EZ33-BM and EZ33-FSP. (e) Microstructure of EZ33-FSP showing refined grains and broken secondary phases uniformly distributed in α-Mg along with line and spots where EDS analysis was performed. (f) Variation of EDS spectra along the line shown in (e) from top to bottom.

(d)

Element (wt. %)	Spot #					
	1	2	3	4	5	6
Mg	97.9	68.4	88.2	95.5	88.1	69.1
Zn	1.3	11.4	2.8	1.8	3.8	6.3
Zr	0.4	0.3	8.6	1.5	2.1	24.4
La	0.1	7.9	0.1	0.5	2.3	0.1
Ce	0.3	12.1	0.3	0.7	3.8	0.2

Eosin stain. Stained sections were observed using optical microscopy (OM, Zeiss Axiovert 40 Mat, Pleasanton, CA).

3. Results

3.1. Mg alloy implant material

The microstructure of EZ33-BM comprised of T-phase precipitates along the grain boundaries in α-Mg matrix (see Fig. 1(b)) along with Zr-rich precipitates in grains interior. ED line scan spectra of a single grain along the precipitates and α-Mg matrix are presented in Fig. 2. The ED spectra indicated Zn and RE rich composition along the grain boundary precipitates and Zr rich composition in the precipitate located within middle of the grain. Quantification of the composition at three different locations marked in Fig. 2(a) is presented in Fig. 2(d). This confirms Zn, RE rich composition along the grain boundary precipitates (Point 2) and the presence of Zr rich precipitate within grain interior (Point 3). As discussed in Section 2.1, T-phase precipitate in Mg–Zn-RE alloy has been observed to exhibit a varying composition dependent upon alloy composition [78–80]. XRD spectra of the EZ33 base material confirms the presence of RE $(Mg, Zn)_{11}$ T-phase precipitates as shown in (Fig. 2 (c). The microstructure of FS processed EZ33 implant material is shown in Fig. 1(c). Refinement of grains and uniform distribution of precipitates can be observed within the processed implant's microstructure (comparing Fig. 1(b) and (c)). ED line analysis of the microstructure corroborates presence of a uniform distribution of secondary T-phase precipitates in the α-Mg matrix as shown in Fig. 2(e). ED spot analysis shows higher concentration of alloying additions in α-Mg (compare Point 1 and 4 in Fig. 2(d)) indicating higher solid solution content after FSP. The Zr-rich precipitates are also observed to be distributed in the α-Mg matrix proximal to grain boundaries (Fig. 2(e)) and not within grain centers, as observed in the base material (Fig. 2(a)).

The results of ICP analysis on the processed material (Table 2) suggests that the composition of FSPed EZ33 alloy did not change significantly subsequent to processing, when compared to the base material (comparing Tables 1 and 2), with negligible addition of iron. The orientation map obtained through EBSD for EZ33-BM and stir zone is presented in Fig. 3(a) and (b), respectively. The microstructure obtained through EBSD scans is similar to that observed through OM and SEM imaging (Fig. 1). Grain orientations studied through pole figures of the BM and the stir zone are shown in Fig. 3(c) and (d) respectively. The BM shows a random texture with the basal pole (0001) showing peak intensities at several points in the ND-TD plane. During friction stir processing material flow in the stir zone is guided by the compressive stress of tool shoulder and shear stress due to the tool pin. During the severe plastic process that occurs during FSP, the basal pole of Mg alloys is oriented along an ellipsoidal trace surface of the tool pin across stir zone along the midplane [63,65,81]. Near the top and bottom of stir zone, the basal pole is oriented along the ND plane, owing to the compressive action of the tool shoulder [63,65,82]. The stir zone shows a single peak indicating the basal pole (0001) is oriented perpendicular to the tool pin surface, and rotated to an angle of about 45° from PD, as shown in Fig. 3 (d). It should be noted that the EBSD scan was obtained in the SZ towards advancing side, hence the basal pole peak is rotated around ND. Results of texture analysis shows FSP has resulted in a processed material with a basal pole perpendicular to implant edges (extracted from the stir zone) that should enhance corrosion resistance [57,61,62].

Grain size analysis of the processed implant material reveals a 91% reduction and more uniform distribution when compared to the base material as shown in Fig. 3(e). The reduction in grain size is reflected in

the Vickers microhardness measurement, with the processed implant material showing a 10.5% higher microhardness when compared to the base material (Fig. 3(f)). The tensile stress-strain curves of the EZ33 base and FSPed materials are shown in Fig. 3(g). From the tensile response it can be observed that after FS processing the materials shows similar ultimate tensile strength whilst ductility has been enhanced by 85%.

3.2. Degradation performance

3.2.1. In vitro response

Results of the in vitro corrosion of EZ33-BM and FSP specimens are shown in Fig. 4(a). Based on our previous study on the corrosion of EZ33-BM, the alloy displayed dissimilar corrosion characteristics at the start of immersion period where corrosion rates were significantly higher followed by a decrease in corrosion rate, reaching a steady state after seven days [48]. The EZ33-BM exhibited dissolution of Mg matrix around secondary phases present along the grain boundary, leading to loss of secondary precipitates and integrity [48], as observed in Fig. 4(c). Drop test on EZ33-BM showed microgalvanic coupling occurring between the T-phase precipitates and α-Mg matrix. The corrosion front propagates along grain boundaries with evolution of hydrogen, due to Mg dissolution around the precipitate, as shown in Fig. 5(a) and (b). Continuous exposure of the EZ33-BM surface to the corrosion medium resulted in dissolution of α-Mg around the precipitates and eventual trenching and falling of the secondary precipitates (Figs. 4(c) and 5(b). In comparison, the FSPed EZ33 surface subjected to the drop test did not exhibit complete trenching of secondary precipitates as seen in Fig. 5(c). Although few precipitates could be observed to fall out, the scale of these precipitates are much smaller in size compared to the base material (comparing Fig. 5(b) and (c)) and it did not affect the overall FSPed alloy corrosion response. Similar findings were observed on a Mg–Al-RE alloy subjected to friction stir processing, where a relatively uniform surface morphology was observed with minimal localized attack [83]. Refinement of secondary phases and their homogeneous distribution within the α-Mg matrix resulted in a reduction in the local area ratio between the cathodic T-phase precipitates and the anodic α-Mg matrix. This minimized the galvanic corrosion between the matrix and secondary phases leading to a relatively uniform corrosion morphology with minimal trenching around the secondary precipitates. EDS elemental analysis was carried out on the drop test exposed corrosion surface with the distribution of elemental concentrations shown in Fig. 6(a) and (b) for EZ33-BM and FSPed specimens, respectively. The elemental maps show that formation of oxide layer occurs in the immediate surrounding of precipitates in the base material while a consistent distribution of oxygen is observed in FSPed specimen indicating a relatively uniform surface film formation due to the mitigation of galvanic corrosion between the matrix and the refined T-phase precipitates as a result of FSP. This was reflected in the corrosion rate measured from the weight loss method. FSP leads to significantly lower corrosion rates with steady-state corrosion achieved after ~9 weeks. FSPed implant material was immersed for a total of 12 weeks from which a calculated corrosion rate was 0.35 ± 0.02 mm/yr was obtained. Weight-loss measurements for base material were discontinued after 2 weeks due to the substantial decrease in size and weight of the studied material, compromising its mechanical integrity (Fig. 4(b)). The calculated corrosion rate for the base material was 4.73 ± 1.27 mm/yr.

Corrosion behavior was also evaluated using EIS. Fig. 7(a) illustrates the evolution of OCP of EZ33 BM and FSPed condition as a function of immersion time and both the conditions exhibit vastly different trends. The OCP for EZ33-BM starts at a value of −1715 mV and increases

Table 2
Chemical composition of EZ33A Mg alloy after subjecting to FSP.

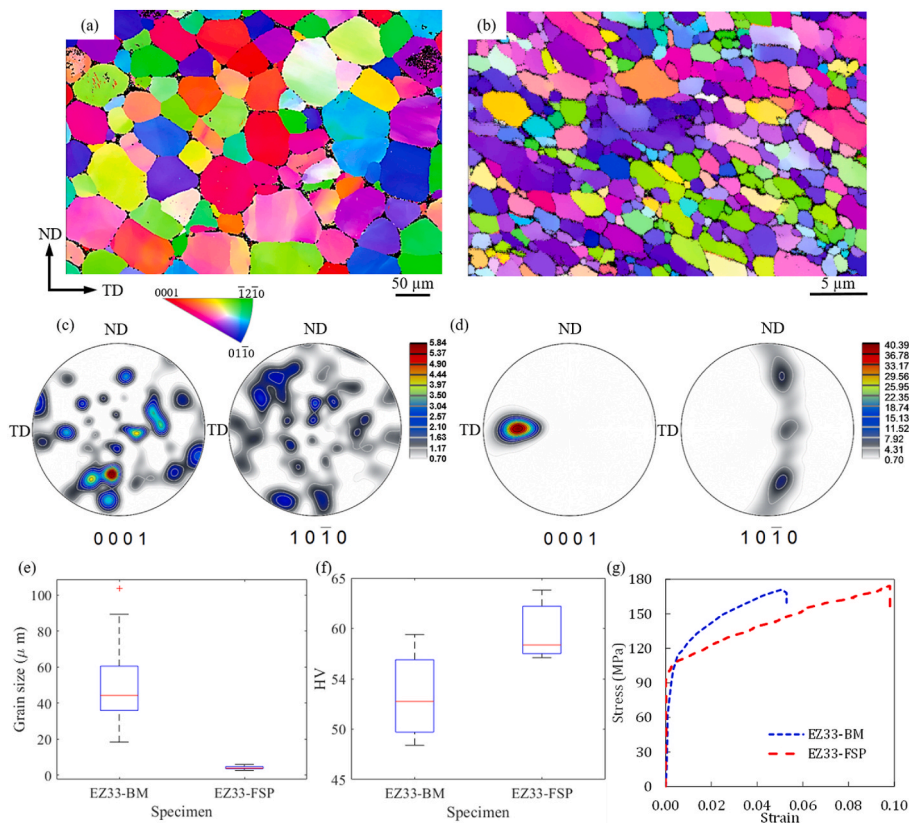| Element	Zn	Zr	Ce	La	Nd	Mn	Fe	Cr	Mg
Wt.%	2.05	0.64	1.08	0.41	0.25	0.01	0.1	<0.01	Balance

Fig. 3. EBSD images showing orientation map in (a) base material and (b) stir zone. Pole figures obtained from orientation images for (c) base material and (d) stir zone. (e) Grain size and (f) Vickers microhardness of as-received EZ33-BM and FSPed EZ33. (g) Tensile stress-strain curves of EZ33 base and FSPed material. EZ33 base material tensile stress-strain curve is obtained from Ref. [47].
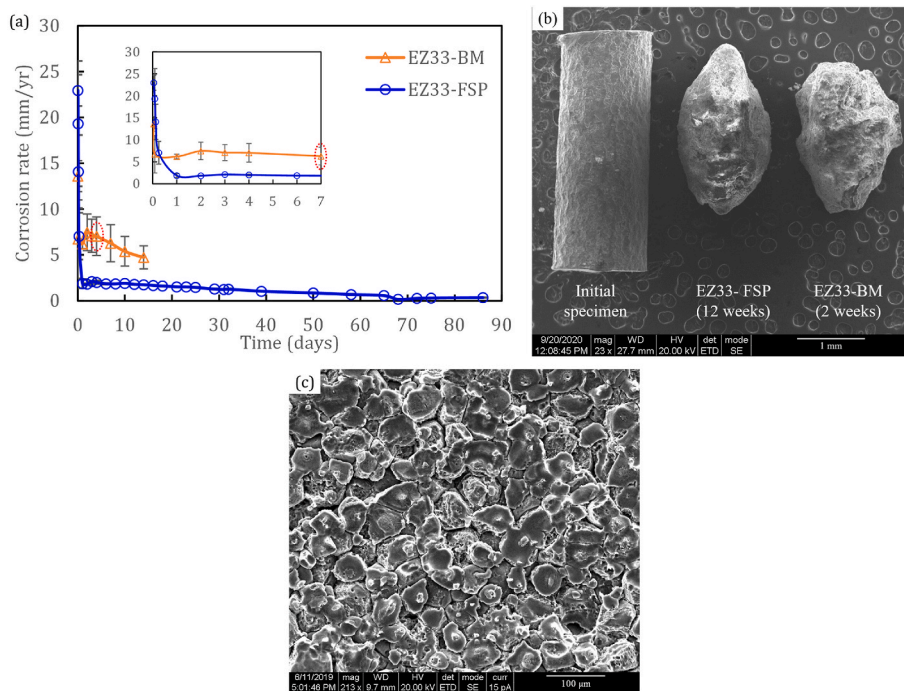

Fig. 4. (a) In vitro corrosion rate of EZ33-BM and FSP material immersed in HBSS. (b) SEM micrograph of initial in vitro specimen, FSPed EZ33 and EZ33-BM specimens immersed in HBSS for 12 and 2 weeks, respectively. (c) SEM image showing microstructure of as-received in vitro EZ33 specimen exposed for 7 days corresponding to data point marked in (a).
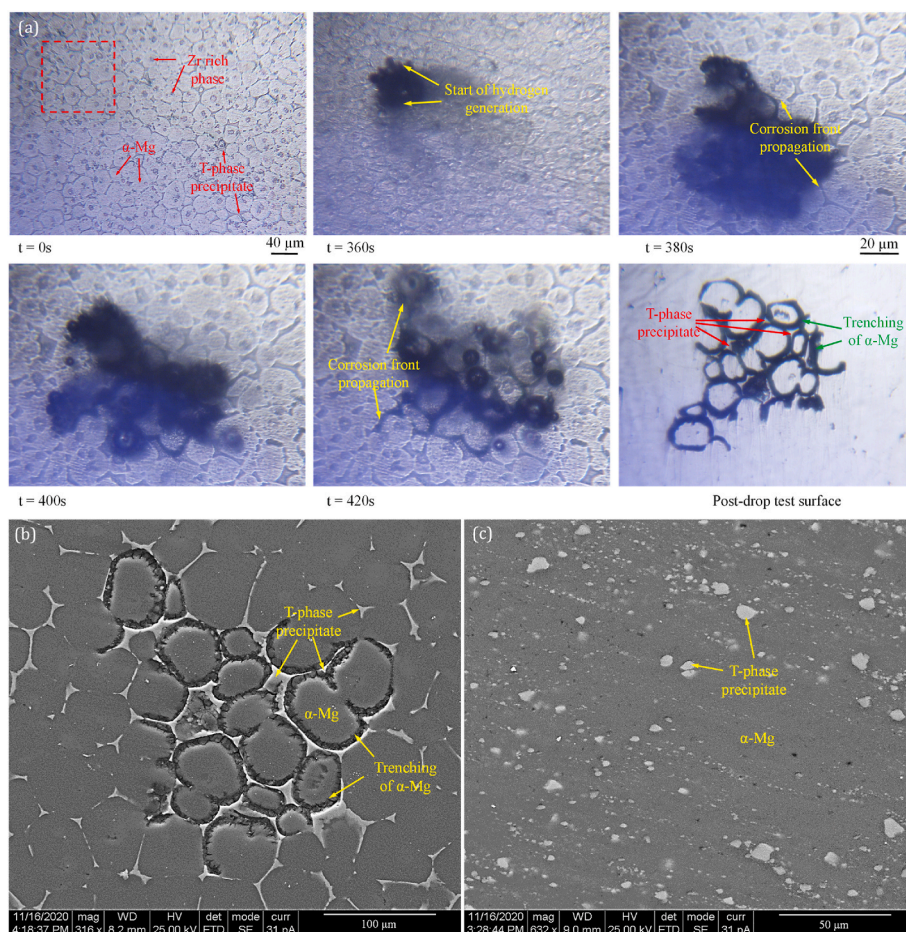
Fig. 5. (a) Chronological drop test images showing corrosion front propagation in EZ33-BM. The corrosion front moves along the precipitates in the grain boundaries. Post drop test corrosion surface of (b) EZ33-BM showing anodic matrix around the T-phase precipitates being preferentially attacked by corrosion and (c) EZ33-FSP material showing uniform corrosion.

rapidly showing the initiation and progression of corrosion until an equilibrium state is reached at the surface. Comparatively, the OCP for FSPed EZ33 does not present significant variability during the 24 h immersion period, though a slight decrease is observed at the start of immersion followed by a continued increase in OCP after approximately 700 min. Towards the end of 24 h of immersion period, OCP of FSPed EZ33 appears to continue increasing whilst a slow decline is noticed for BM. This behavior is indicative of progressive formation of a stable surface film on FSPed EZ33 surface, and also suggests that surface film formed on BM was unable to maintain stability. The variation in slopes between start and end of immersion, demonstrates inability of the surface film forming on EZ33-BM to maintain its integrity. It should be noted that initially, FSPed EZ33 presented nobler OCP values than the base material which may be attributed to the higher RE content in α-Mg grains in FSPed sample due to the disintegration and dissolution of secondary phases back into the matrix (Fig. 2). However, towards the end of immersion period, the potential of EZ33-BM becomes more positive which may relate to relatively higher reactivity of the surface at immersion experiment start.

Fig. 7(b) shows PDP curves for base material and FSPed samples after 24 h of immersion. Corrosion rates measured using PDP curves were 0.4 mm/yr and 0.15 mm/yr for EZ33 BM and FSPed condition, respectively. The trend is similar to corrosion rates calculated by weight loss measurements, albeit with minor disparities due to variation in exposure area between the two techniques. The corrosion potential, E_{corr}, for both samples is similar, as indicated by OCP measurements. Variation in corrosion rates may be attributed to the difference in anodic and cathodic kinetics. A 'passive window' can be seen at E_{corr} of approximately −1.3 V vs. Ag/AgCl in the PDP curve for FSPed EZ33. The presence of passivation in the anodic branch of FSPed EZ33 is a result of a partially protective film forming on FSPed sample surface. This was also observed in OCP curves. Nyquist plots from EIS data for both samples are plotted in Fig. 7(c) and (d), which were used to study the corrosion behavior at different timepoints as well as the developed surface film. The proposed equivalent circuit model used for fitting the EIS data is shown in Fig. 7(e) where the high frequency capacitive loop is attributed to double layer capacitance in parallel with the charge transfer resistance while the mid-frequency capacitive loop is related to the surface film formed on the Mg alloy. On the other hand, the inductive loop in the low frequency range modeled the behavior of the absorbed/desorbed species on the metal surface. The fitting results for the selected EIS measurements are presented in Table 3. EIS spectra for both samples showed two capacitive loops at high and intermediate frequency ranges, as well as inductive loop at low frequency ranges. This is typical of Mg alloy corrosion, where the diameter of the capacitive loop is an indication of the charge transfer resistance. The charge transfer resistance of EZ33-BM continued to increase for the first 5 h, indicating that an oxide layer was forming on the surface and therefore increasing corrosion resistance of the material (Fig. 7(c)). However, after 5 h of immersion, a decrease in the diameter of the capacitive loop is observed until it reaches ~40% of its initial resistance value. The developed surface film was weak and decrease in resistance signifies its disintegration, resulting in high corrosion rates after 24 h of immersion, as evidenced by weight loss and EIS fitted results. Conversely, FSPed
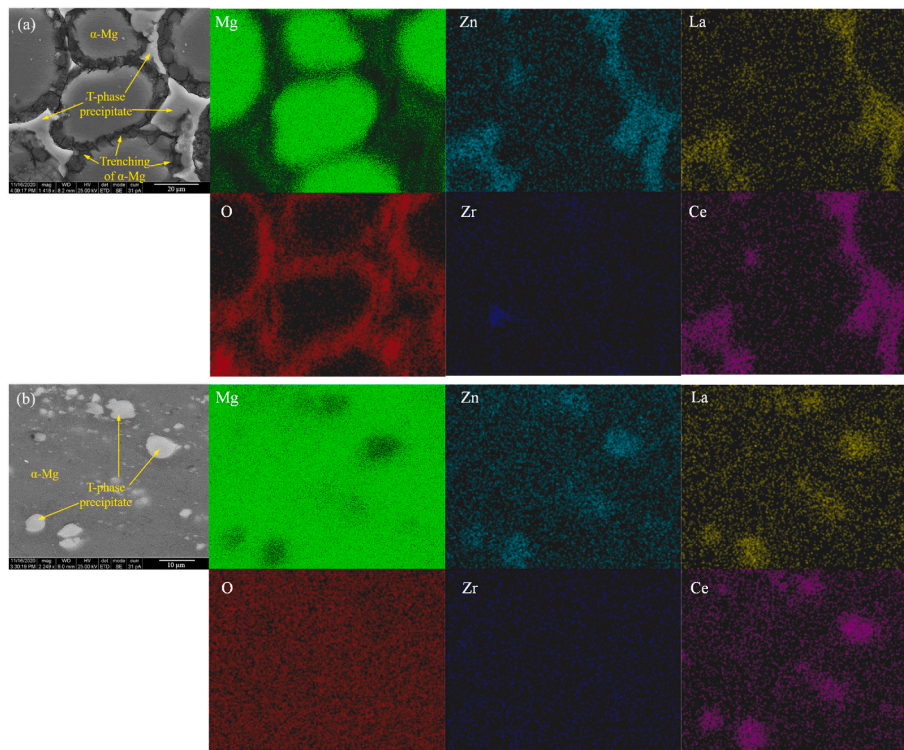
Fig. 6. EDS elemental mapping on the post drop test corrosion surface showing distribution of different elemental compositions (a) EZ33-BM and (b) EZ33-FSP. The uniform distribution of oxygen shows a consistent passivation layer forming in EZ33-FSP specimen, compared to EZ33-BM specimen.

condition (Fig. 7(d)) offered lower resistances than the base material, though resistances increase steadily with progressive immersion until it reaches 1.5 times its initial value after 24 h, which was higher than the base material. Furthermore, the surface film resistance of FSPed EZ33 increased throughout the immersion time compared to EZ33-BM whose film resistance decreased to ~40% of its initial resistance value. The progressive increase of both charge transfer and film resistances confirm the development of a stable oxide layer forming on the FSPed sample surface capable of maintaining its integrity throughout the immersion time. The capacitive values of the double layer (C_{ct}) and surface film (C_f) were also calculated from the equivalent circuit model (Table 3) and presented higher and less stable values for EZ33-BM, further confirming stable surface film formed on FSPed sample. Film thickness was determined from the effective dielectric film capacitance values (C_f) for ideal capacitors (Table 3) and confirmed that the film thickness developed in the FSPed sample was approximately double the thickness of that formed on BM surface.

3.2.2. Cytotoxicity

Cytotoxicity tests were performed to understand the biocompatibility of EZ33 and compare it with that of its main rare earth alloying elements: Nd, La and Ce. Fig. 7(f) shows the cell viability cultured for eight days in two different mediums: DMEM + 10% FBS and DMEM + 25% FBS + 10% DMSO, where the latter served as the positive control. As mentioned previously, there have been concerns about utilizing rare earths in biodegradable applications due to their toxicity [84]. Based on the results shown in Fig. 7(f), cerium displayed the lowest cell viability, followed by neodymium and lanthanum, having comparable yet higher absorbance levels. These results agree with those reported by Feyeraband et al., in which eight REs were tested, with Ce being found to be a highly toxic element, significantly affecting cell viabilities, followed by lanthanum and neodymium [85]. Conversely, cells cultured in EZ33 alloy extracts showed a significant higher absorbance than the rare earth elements, demonstrating that there was good cell growth. This was expected given the fact that these elements are present in EZ33 in trace amounts (Table 1). Therefore, it is possible for RE-based Mg alloys to actually promote cell growth as long as the RE present in the alloy are within tolerable concentrations to prevent cytotoxicity [86]. Feyeraband et al. attempted to determine these levels by testing the biocompatibility of Ce, Er, La, Gd, Nd and Y and reported the half-lethal dose which is the concentration in mg/kg of each element that would result in the loss of 50% of cultured cells [85]. Comparing these results with the addition of DMSO in the second medium, which is known to damage living cells, a significant reduction in absorbance levels were noticed across all extracts except for cerium. Since cerium has proven to be highly toxic, the minor addition of 10% DMSO did not have a significant impact upon cell viability. However, even with the deliberate action of destroying living cells, EZ33 showed the highest cell viability levels compared to pure rare earth extracts, further establishing cytocompatibility of the alloy. According to ISO 10993-5, EZ33 exhibits Grade 0 cytotoxicity suggesting that it is an eligible material for biological applications [74].

3.2.3. In vivo response

The present study has been designed in such that control animal models would be subjected to exact surgical procedure as implant group, with the exception of receiving implant material, providing a measure of the bone healing time period. μCT scan images of bone healing in control animal models are shown in Fig. 8(a). It can be observed that bone recovers restitutio ad integrum by eight week post-procedure. Stage 2 of bone healing [87,88]: formation of fibrocartilaginous callus, can be observed, marked by an arrow in the μCT orthoslices shown in Fig. 8(c). Further to this, Stage 3 of bone healing [87,88]: formation of bony callus, can be observed in the μCT orthoslices presented in Fig. 8(d), followed by bone remodeling (Fig. 8(d)). The control group in the present study suggests that bone healing occurs over a time period of eight weeks, which approximates to the time period observed for bone healing in pediatric patients [27,89]. The control group, aids the establishment of a base time period over which the implant material needs to have a stable corrosion rate, whilst creating no discernible inflammation or
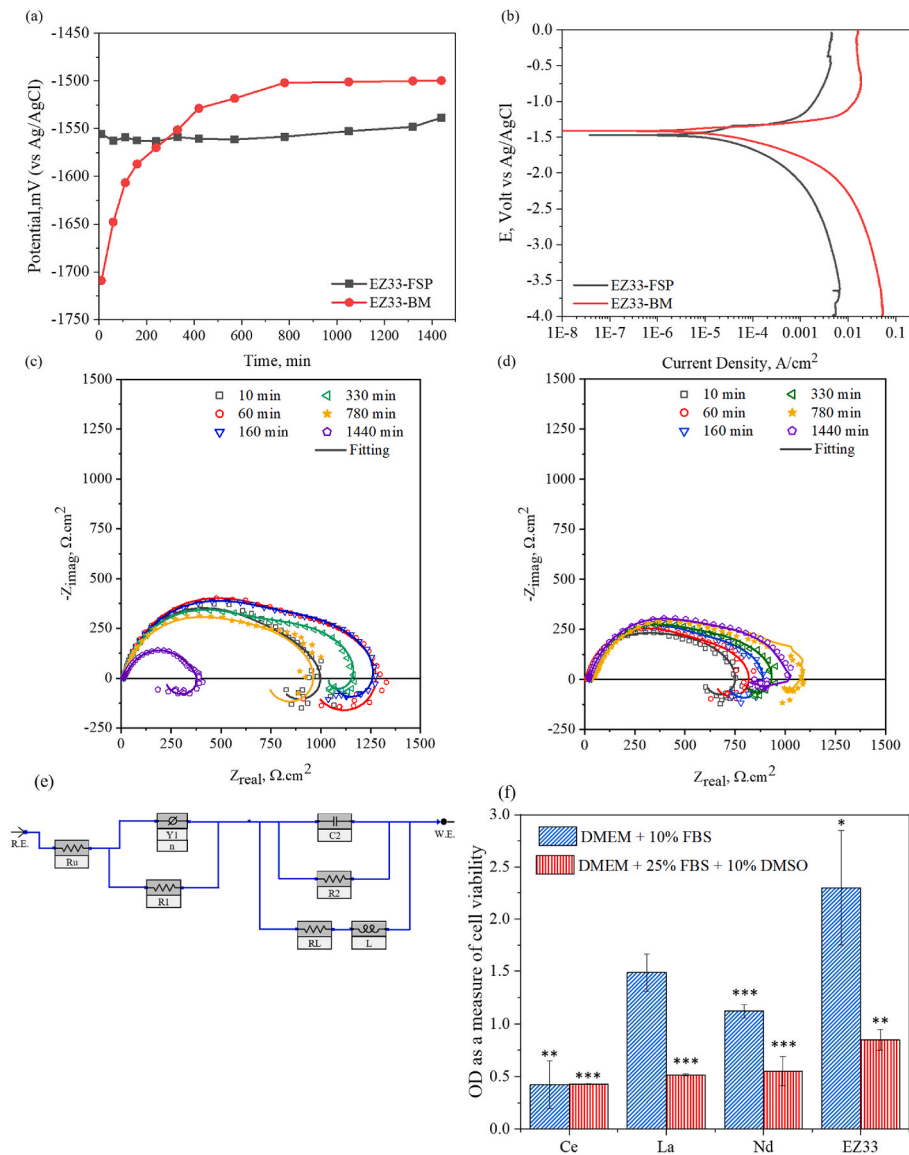
Fig. 7. (a) Evolution of open circuit potential of base material and FSPed EZ33 alloy exposed to HBSS for 24 h, (b) Potentiodynamic polarization curves and (c) and (d) Nyquist plots for base material and FSPed EZ33 alloy, respectively. (e) Equivalent circuit utilized for sitting EIS data for both EZ33 BM and FSPed materials during different time intervals. (f) Results of cytotoxicity – cell viability cultured for a period of eight days.

Table 3
Fitting results for EIS measurements made on EZ33 base material and friction stir processed in HBSS at open circuit potential at different immersion time, as per the equivalent circuit shown in Fig. 7(e).

| Time min	R_{ct}, Ohm.cm$^2 \times 10^2$		R_f, Ohm.cm$^2 \times 10^2$		Capacitance (C_{ct}), F/cm$^2 \times 10^{-5}$		Capacitance, (C_f)F/cm$^2 \times 10^{-5}$		Film thickness nm		RL, Ohm.cm$^2 \times 10^2$		L H.cm$^2 \times 10^3$	
EZ33 alloy	BM	FSP	BM	FSP	BM	FSP	BM	FSP	BM	FSP	BM	FSP	BM	FSP
10	5.67 ± 0.24	5.77 ± 0.13	4.63 ± 0.24	2.15 ± 0.18	4.13 ± 0.04	4.79 ± 0.03	2.89 ± 0.07	5.77 ± 0.22	0.30 ± 0.01	0.15 ± 0.04	0.40 ± 0.08	0.67 ± 0.02	6.13 ± 0.09	1.20 ± 0.18
60	9.07 ± 0.36	5.87 ± 0.21	5.19 ± 0.28	3.17 ± 0.18	4.99 ± 0.17	5.02 ± 0.01	3.68 ± 0.15	4.43 ± 0.21	0.24 ± 0.06	0.20 ± 0.04	0.59 ± 0.04	0.76 ± 0.03	3.33 ± 0.49	2.04 ± 0.03
160	10.05 ± 0.51	6.37 ± 0.19	4.69 ± 0.27	3.38 ± 0.20	4.69 ± 0.16	5.23 ± 0.05	4.18 ± 0.19	4.31 ± 0.21	0.21 ± 0.05	0.20 ± 0.04	0.80 ± 0.06	0.77 ± 0.01	1.97 ± 0.40	2.01 ± 0.34
330	9.63 ± 0.61	6.84 ± 0.22	4.32 ± 0.22	3.15 ± 0.23	5.08 ± 0.19	4.97 ± 0.02	3.91 ± 0.16	4.67 ± 0.26	0.22 ± 0.05	0.19 ± 0.03	1.15 ± 0.08	1.41 ± 0.05	1.79 ± 0.44	2.45 ± 0.52
780	7.23 ± 0.15	8.57 ± 0.29	3.06 ± 0.19	3.71 ± 0.20	5.03 ± 0.22	7.89 ± 0.07	4.44 ± 0.16	3.81 ± 0.22	0.20 ± 0.05	0.23 ± 0.04	1.85 ± 0.23	1.29 ± 0.22	1.29 ± 0.27	2.47 ± 0.46
1440	2.14 ± 0.14	8.85 ± 0.95	1.74 ± 0.11	3.55 ± 0.34	6.49 ± 0.06	7.38 ± 0.04	5.89 ± 0.05	3.08 ± 0.42	0.15 ± 0.02	0.28 ± 0.02	2.16 ± 0.14	3.40 ± 0.15	6.05 ± 0.10	0.822 ± 0.14
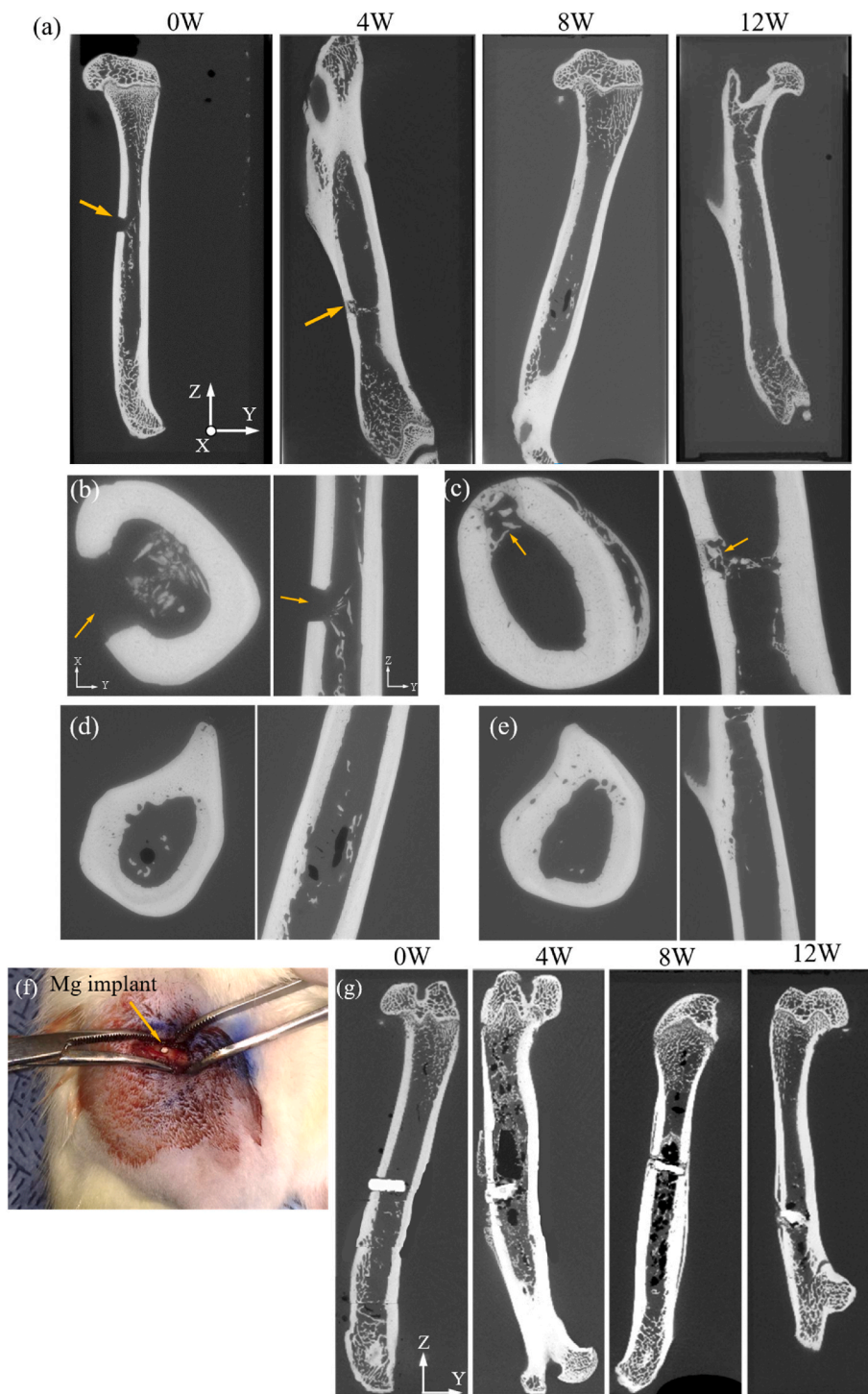
Fig. 8. (a) μCT orthoslices of femur bones of control group showing bone healing by Week 8. (b) Higher magnification of hole drilled in femur at Week 0, (c) fibrocartilaginous callus formation in Week 4 specimen – Stage 2 of bone healing [87,88], (d) bony callus formed in Week 8 specimen – Stage 3 of bone healing [87,88] and (e) bone remodeling in 12-week specimen – Stage 4 of bone healing [87,88]. (f) Implantation of FS processed EZ33 implant in the rat femur animal model and (g) μCT orthoslices showing degradation of friction stir processed EZ33 implants at different time periods.

toxic corrosion products. Following this, corrosion of the processed implant material is accessed and the corrosion rate is juxtaposed with the established healing time period.

The FSPed EZ33 implant material was inserted transcortically into the rat femur as shown in Fig. 8(f), and was well tolerated by all animal models. No swelling or infections were observed around implant site, and the animals behaved and fed normally throughout the study period (12 weeks). This was reflected in their weights measured during euthanasia: male – 679.6 ± 54.8 g; female – 347.8 ± 35.9 g. The in vivo corrosion of inserted implant was monitored through μCT imaging at regular intervals (0, 4, 8 and 12 weeks) throughout the study time

period, with representative 2D orthoslices for the respective in vivo time intervals (i.e. 4, 8 and 12 weeks) presented in Fig. 8(g). The images evidence varying degrees of corrosion on the implants. The processed EZ33 material resulted in increased bone formation around the implant from weeks 4–12, as can be seen in Fig. 8(g). Gas evolution due to corrosion of the implanted material is minimal and did not ostensibly affect bone regeneration. New bone formation occurred around the implant in the cortical and medullary cavity areas from 4 weeks, as can be seen in Figs. 8(g) and 9(a)–(f). Histological slices of the implanted femur showed active bone growth with osteoblastic activity (osteoblasts and osteocytes) around the implant site at four weeks (Fig. 9(b)). At
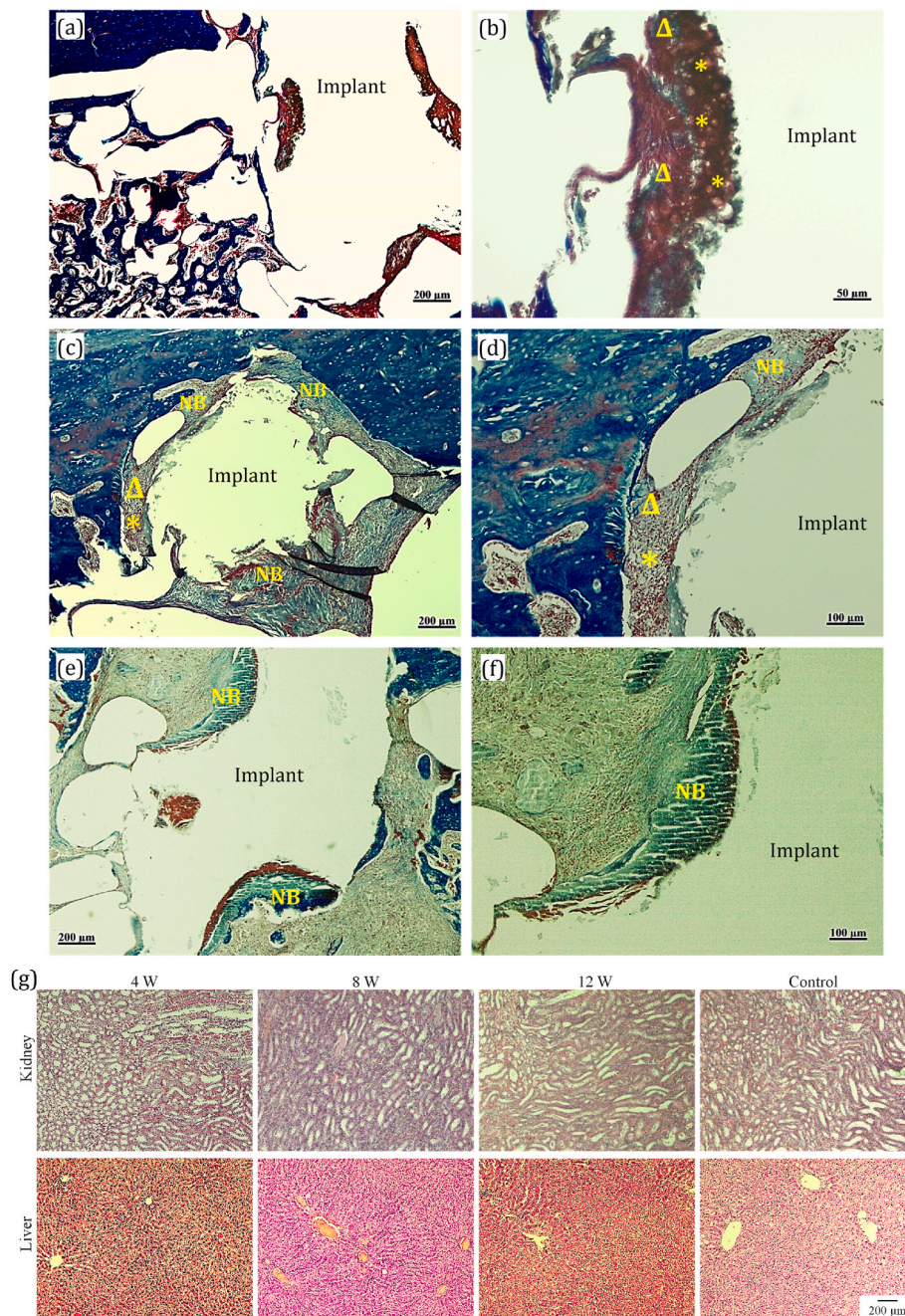
Fig. 9. Histological slices of FSPed EZ33 Mg implanted rat femur in Masson's trichrome stain after (a), (b) Week 4, (c), (d) Week 8 and (e), (f) Week 12 in vivo study period. At Week 4 osteoblasts (*) are observed around the implant, Week 8 shows osteocytes (Δ) and new bone (NB) formation around the implant and Week 12 shows new bone around the implant. (g) HE stained histological slices of kidney and liver for different sampling interval compared with control (Week 12) specimen.

eight weeks, new bone formation could be observed around the implants (Fig. 9(d)), and at 12 weeks the implant was completely surrounded by bone growth (Fig. 9(f)).

The CT scan slices were processed to segment the implant at different time intervals. The resulting segmented images of the in vivo corroded implants at different time intervals are shown in Fig. 10(a). The implant volume is calculated and is utilized to derive the in vivo corrosion rate of FS processed EZ33 implant material using Eq. (2). Implant volume at different time intervals and associated in vivo corrosion rates are presented in Fig. 10(b) and (c), respectively. The implant volume changed until week eight and maintained a constant value until end of present study (12 weeks), having a similar trend to that inferred from in vitro weight loss measurements (Fig. 6(a)). The corrosion rate maintained at

an average of 1 mm/year until eight weeks, decreasing to 0.7 mm/year until the end of the study's duration. The evaluated implant volume (normalized with respect to the initial implant volume) and corrosion rate are compared with different Mg alloys (WZ21 (Mg–Zn–Ca–Y), ZX50 (Mg–Zn–Ca) and ZX50-MAO (micro arc oxidized)) from the existing literature [5,89], as shown in Fig. 10(d) and (e), respectively. The FSPed EZ33 alloy showed in vivo corrosion properties that fall between the two aforementioned Mg alloys: i.e. fast corroding ZX50 and slow corroding WZ21 [5,89]. Notably, comparison of the in vivo corrosion rate of FSPed EZ33 with that of different Mg alloys (Fig. 10(f)) [5,8,89–91], reveals superior corrosion properties for the candidate implant material. It is to be observed here that the in vivo corrosion rates obtained from literature [8], for the different Mg alloys can have variability due to processing
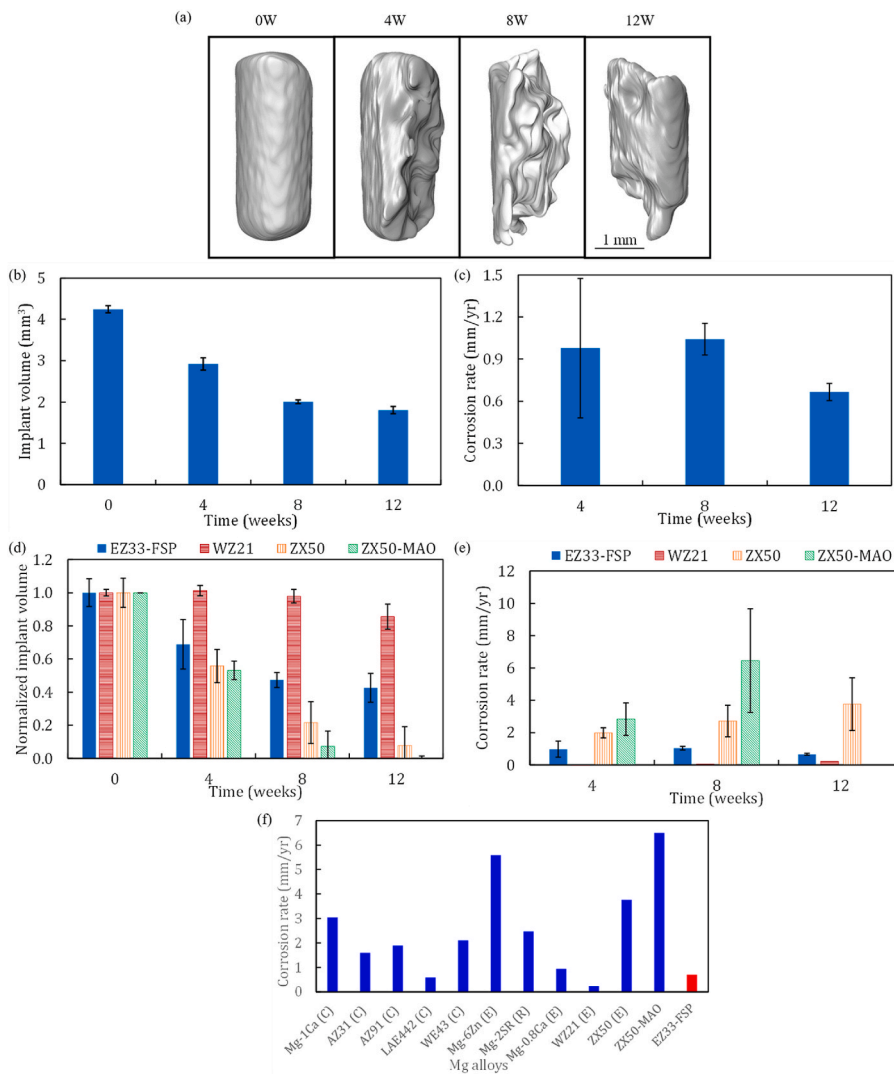
Fig. 10. (a) Segmented in vivo corroded EZ33-FSP implants at different time intervals. Variation of (b) implant volume and (c) corrosion rate calculated based on µCT orthoslices showing EZ33 implant degradation performance over the tested period. Comparison of (d) normalized implant volume (implant volume at particular time/initial implant volume) and (e) corrosion rate calculated based on in vivo implant volume loss over the exposed time period. Data for alloys WZ21, ZX50 and ZX50-MAO are obtained from Refs. [5,89]. (f) Comparison of in vivo corrosion rate of different Mg alloys [5,8,89–91], (C) – as cast; (E) – extruded; (R) – rolled; MAO – micro arc oxidized; FSP – friction stir processed.

conditions and exposure to different corrosion environment [8,92].

Although no inflammation and high gas evolution were observed around the implant site, the functionality of critical organs (kidney and liver) were analyzed by performing blood serum analysis. The blood serum was analyzed for Mg, Urea, Ca, blood urea nitrogen (BUN) and enzymes (Alanine aminotransferase (ALT), Aspartate aminotransferase (AST), Alkaline phosphatase (AP) and creatinine, (Fig. 11). The results of blood work subjected to Mann-Whitney U statistical test with a *p* value of 0.05, showed that there was no significant difference between the control and implant groups at each sampling interval. Moreover, histological slices of the critical organs (kidney and liver) substantiated blood serum analysis results, showing normal tissues at each sampling interval (Fig. 9(g)). These results suggest that degradation of the FS processed EZ33 Mg alloy did not adversely affect the functionality of the animal model's critical organs over the study period.

4. Discussion

The utilization of Mg–Zn–RE–Zr alloy (EZ33) for biomedical applications has been studied by subjecting the alloy to severe plastic deformation, engineering the microstructure to simultaneously improve mechanical and corrosion properties. FSP resulted in refined grains in the stir zone that resulted in improved microhardness. The mechanical properties of Mg alloys have been shown to exhibit a Hall-Petch relationship, with decreasing grain size leading to improvements in

hardness [93,94]. Venkataiah et al., performed FSP of Mg–Zn–Zr-RE alloy ZE41 and observed an average grain size of 3 µm in the processed region compared to 110 µm within the initial material, resulting in a 15% increase in microhardness in the processed material [95].

The tensile stress-strain curves of the EZ33 base and FSPed materials are shown in Fig. 3(g). From the tensile response it can be observed that after FS processing the materials shows similar strength whilst ductility has been enhanced by 85%. The mechanical properties of severe plastically deformed Mg alloys are dependent on factors such as grain size, grain boundary character and texture [63,68,81,96]. Mg alloys subjected to FSP have shown considerable increase in ductility with similar or even enhanced strength [68,97–100]. Although FSPed material showed a fine grain microstructure compared to the starting base material (Fig. 3(e)), the strength of processed material was similar to the base material. Kumar et al., studied effect of microstructure on tensile response of Mg-RE alloy WE43 by subjecting to FSP [68]. The study also made a similar observation under tensile loading, with increased ductility and similar strength for processed material compared to base material. It was reported that the alloy strength was influenced by presence of high angle grain boundaries and microstructural and texture analysis showed similar boundary spacing for base material and FSPed material [68]. In addition, the precipitates similar to the present alloy are located along the grain boundaries and did not contribute to strength [68]. Wang et al., also reported that FS processed Mg alloy exhibited weak yield strength – grain size dependence due to the evolved texture
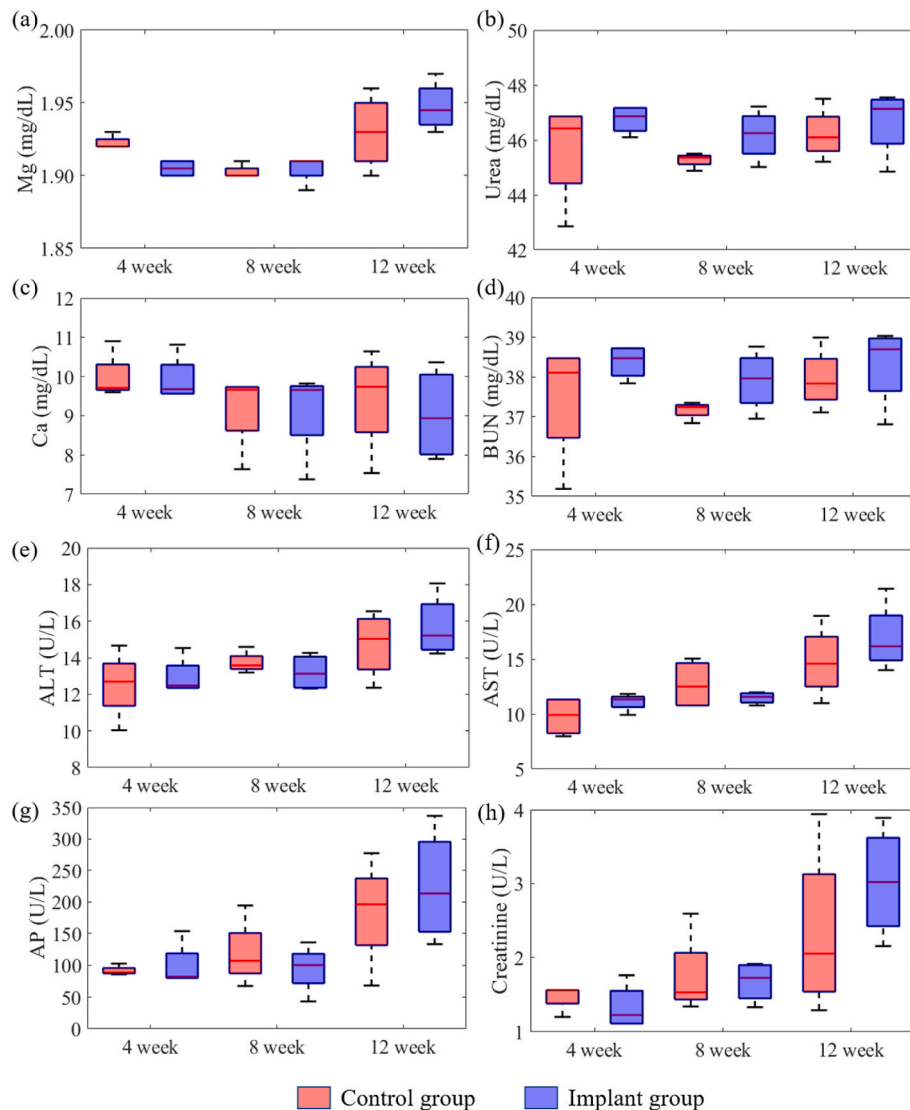
Fig. 11. Results of blood serum analysis showing variation of (a) Mg, (b) urea, (c) calcium and (b) blood urea nitrogen (BUN) and different enzymes (e) Alanine aminotransferase (ALT), (f) Aspartate aminotransferase (AST), (g) Alkaline phosphatase (AP) and (h) creatinine, with respect to duration of implantation for control and implant groups.

in HCP Mg alloy post FSP [81]. Hence improvement in strength post FSP was not observed while ductility showed remarkable increase. The increase in ductility through FSP is attributed to the evolved texture in the stir zone and activation of non-basal slip systems [81,97,98].

The alloys electrochemical response under in vitro conditions showed improved passivation owing to refined grain size, uniform distribution of secondary phases and preferred texture. The in vivo component of the study was performed with an aim to establish a time frame for the alloy to support bone regeneration. This could have profound implications for pediatric long bone fracture management. To understand corrosion of the processed alloy material under in vivo conditions, transcortical model implantation is preferred [5,89], since it provides insights into the corrosion response to both cortical bone and marrow. Based on the present study, three major findings can be ascertained for the application of Mg based alloys for clinical applications:

- FSP grain refinement, uniformly distributed secondary phases and preferred basal texture inhibit corrosion process.
- FSP results in more uniform corrosion in Mg alloys.
- Steady release of Mg ions aids implant-bone interface development.

The results will be discussed in detail based upon these three findings.

4.1. FSP – grain refinement, uniform distribution of secondary phases and preferred basal texture – inhibit corrosion process

In the literature, several techniques such as coatings and/or depositions have been explored to control the biodegradability of Mg alloys [8,101–103]. However, in such methods there is always a chance of poor performance if the coating is broken, resulting in the exposure of the base metal and excessive corrosion. Moreover, the coating should be selected such that no toxic reaction products are released due to its dissolution. To improve corrosion resistance and control biodegradability of Mg alloys, microstructure engineering (grain size, distribution of secondary phase and texture) through friction stir processing provides improved control of the entire alloy microstructure. FSP resulted in a dominant basal texture in addition to refinement of grains and uniform distribution of secondary phases. Studies have shown that Mg alloys with a preferred basal orientation have exhibited greater corrosion resistance [57,61]. In vitro (EIS and OCP) results on EZ33 alloy showed formation of surface oxide layer upon exposure to HBSS and the stability

of layer remained intact with time offering higher stability in the FSPed specimen when compared to BM.

4.2. FSP results in more uniform corrosion in Mg alloys

In vitro corrosion of EZ33-BM in HBSS showed that secondary phases acted as cathodic sites to anodic α-Mg, resulting in anodic dissolution and eventual loss of precipitates, as shown in Fig. 4(c) [48]. Subjecting the alloy to FSP resulted in a microstructure with refined grains, preferred texture and uniformly distributed secondary precipitates. In vitro weight loss corrosion exposure of as-received specimens led to specimen disintegration by nearly half its initial volume within the first two weeks, resulting in BM weight loss experiments being halted prematurely (Fig. 4(a)). However, the FSP EZ33 specimen's corrosion was relatively uniform (Fig. 7(a)) since the precipitates had been broken and uniformly distributed in the α-Mg matrix as can be seen in Fig. 2. The relatively uniform corrosion observed in the FSP EZ33 specimen compared to base material, is a result of refined grains, broken and uniform distribution of secondary precipitates and preferred basal texture.

The implant specimen subjected to 12-week in vivo corrosion was analyzed using SEM fitted with EDS to study compositional variation occurring at the bone-implant interface and within its immediate vicinity. The in vivo embedded implant surface was lightly polished and etched with acetic picral solution to reveal the microstructure and is shown in Fig. 12(a). Critically, microstructure of the 12 week in vivo corroded implant (Fig. 12(a)) looks similar to the FS processed implant microstructure (Fig. 1(c)). In the case of as-received EZ33 alloy, when exposed to HBSS, dissolution of α-Mg occurred, resulting in loss of secondary precipitates (comparing EZ33-BM alloy in vitro corroded microstructure in Fig. 4(c) with initial microstructure in Fig. 1(b)). Exposing this alloy system in BM condition could result in excessive release of precipitate elements (i.e., RE, Zr and Zn) (Fig. 2(f)) into the animal model leading to toxicity. In the FS processed sample, secondary precipitates were broken down and uniformly distributed, with some of the alloying elements dissolved back into the α-Mg matrix resulting in an α-Mg solid solution (comparing α-Mg composition – Point 1 and 4 in Fig. 2(d)).

To evaluate compositional changes on the in vivo corroded implant, an EDS scan was performed along the line depicted in Fig. 12(a). ED line scan analysis (Fig. 12(b)) shows dispersion of T-phase precipitates in α-Mg matrix similar to the FS processed alloy (Fig. 2(f)). ED spot analysis of α-Mg and precipitates on the in vivo corroded implant (Point A and B in Fig. 12(a) respectively), is presented in Fig. 12(c). Comparing the
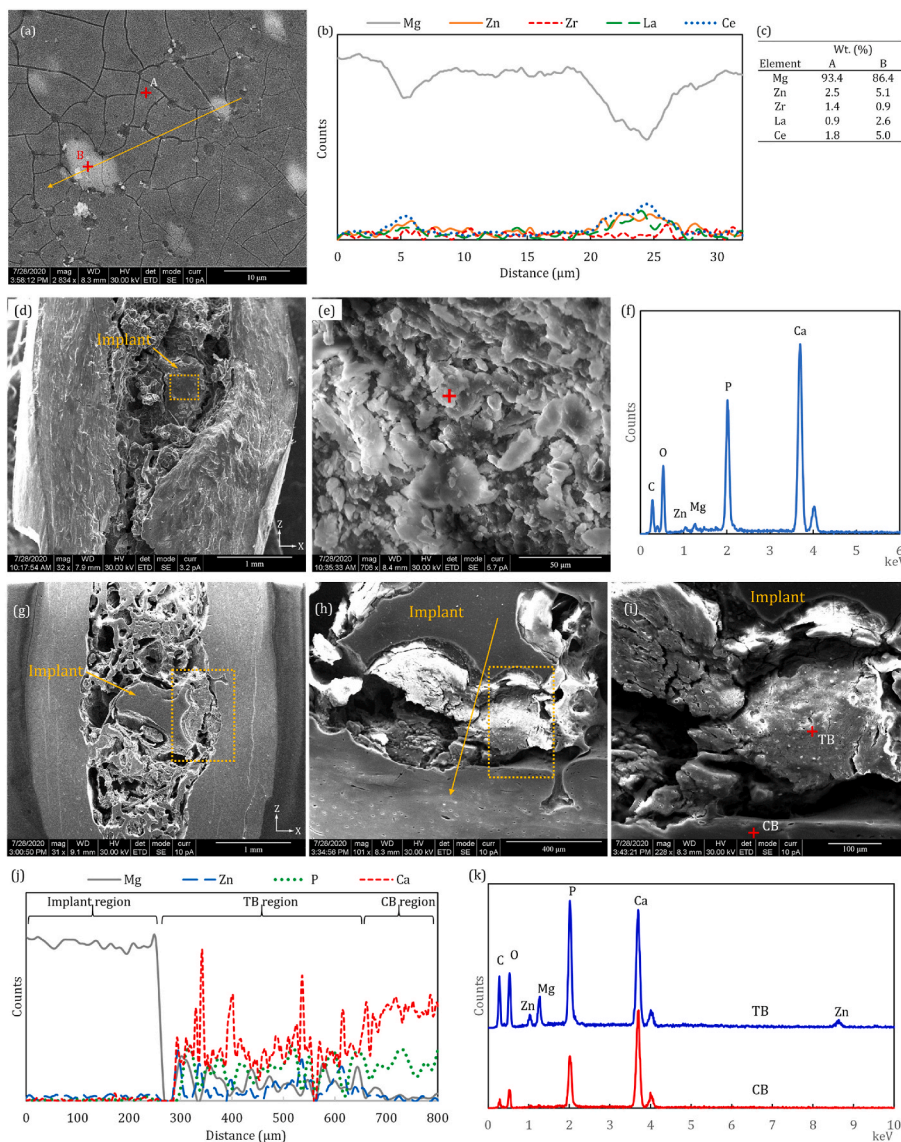

Fig. 12. (a) SEM image showing precipitates in α-Mg matrix in Week 12 implanted in vivo specimen, (b) ED line spectra obtained along line shown in (a) and (c) variation of elemental composition based on EDS obtained at points A and B marked in (a). (d) Cross section of implanted bone specimen harvested after Week 12, showing implant-bone osseointegration, (e) magnified image of implant in marked region shown in (e). (f) ED spectra obtained at point marked in (e) showing calcium and phosphorus indicating osseointegration and new bone formation around implant. (g) Slight polishing of specimen shown in (d) to reveal the actual implant. (h) Higher magnification of marked implant-bone interface in (g). (i) Trabecular bone formation around implant from marked region in (h), (j) ED line spectra along line shown in (h) and (k) ED spectra obtained at points on trabecular bone (TB) and cortical bone (CB), shown in (i).

composition of α-Mg (point A) and precipitate (point B) in the in vivo corroded specimen (Fig. 12(c)) and FSP implant specimen (Fig. 2(d)), it could be observed that content of Mg is lower in in vivo corroded specimen. Corrosion of Mg within an aqueous medium occurs by anodic dissolution and cathodic reduction of Mg metal, resulting in formation of $Mg(OH)_2$ and evolution of hydrogen gas [16]. Exposure of FSPed EZ33 alloy under in vivo condition shows that dissolution of Mg occurs uniformly throughout the entire implant with the corrosion rate around 1 mm/year until eight weeks, eventually reducing to 0.7 mm/year. The corrosion of the implant occurs more within the medullary cavity compared to the cortical region of the bone as observed in Figs. 8(g) and 10(a). Similar observation has been made by Kraus et al., during in vivo study of ZX50 and WZ21 Mg alloy implants [89]. This behavior can be attributed to higher vascularization, with the presence of blood vessels in the bone marrow removing implant degradation products and balancing the local pH. Although corrosion was higher within the medullary region, it did not result in any detectable inflammation or toxic reaction products, along with, non-deterrence to new bone formation.

4.3. Steady release of Mg ions – aids implant-bone interface

The 12-week implant group specimen was analyzed with SEM/EDS to study the bone-implant interface for new bone formation and to detect the degree to which implant elements were permeating into the surrounding bone. SEM image of the implanted bone specimen observed in longitudinal cross-section is shown in Fig. 12(d). It can be observed that the implant material is surrounded by new bone formation, in similitude to femur histology slices (Fig. 9(e) and (f)). ED spot analysis of the implant area shown in Fig. 12(e), shows major presence of calcium, phosphorus, carbon, oxygen and some content of magnesium and zinc, as shown in Fig. 12(f). Li et al., utilized EDS analysis to study four weeks in vivo exposed Mg–Ca alloy specimens and observed presence of Ca, P, C and O on the Mg alloy implant surface [104]. Natural bone is a heterogenous hierarchical structure, composed of an inorganic mineral phase (hydroxyapatite), organic phase (collagens) proteins and water [87,105–107]. The mineral phase primarily comprises of amorphous calcium phosphate (hydroxyapatite – $Ca_{10}(PO_4)_6(OH)_2$) along with calcium carbonate [87,105–107]. The presence of bone minerals on the implant surface suggests good osseointegration between bone and the implanted alloy. The 12-week implant specimen was cold mounted and slightly polished to reveal implant, as shown in Fig. 12(g). Higher magnifications of the implant – bone interface is presented in Fig. 12(h) and (i). ED line scan analysis across the implant – bone interface represented by line in Fig. 12(h) and is shown in Fig. 12(j). This analysis shows high content of Mg, Zn elements within the implant region and Ca and P elements in the cortical bone (CB) region (Fig. 12(j)). The trabecular bone (TB) formed around the implant shows varying concentration of elements. To further analyze the composition changes across the implant – bone interface, ED spot analysis was performed on TB and CB at points shown in Fig. 12(i). The ED spot analysis show that content of Mg and Zn is higher in the trabecular bone within the immediate vicinity of the implant, when compared to the cortical bone (Fig. 12(h)). The release of Mg ions along with the deposition of Ca and P on the implant are indications of osteoblastic activity, leading to formation of new bone around the implant site [44,104,108].

4.4. Outlook

Results from the present study suggest FSPed EZ33 alloy to be a suitable implant material for pediatric patients and can eliminate the need for secondary surgeries. Further research is needed to study long term corrosion effects until the implant material is completely degraded along with ICP on internal organs to identify trace element deposition and the corrosion behavior of different implant geometries such as screws, plates and nails.

5. Conclusions

A Mg–Zn–RE–Zr alloy i.e., EZ33 Mg alloy was subjected to friction stir processing and studied for in vitro and in vivo corrosion response and biocompatibility. The following conclusions can be drawn based upon the present study.

1. Friction stir processing of EZ33 Mg alloy resulted in refined grains and a uniform distribution of T-phase precipitates in the α-Mg matrix, resulting in improved hardness and ductility, compared to the base material.
2. In vitro corrosion of the FSPed EZ33 alloy indicated the formation of a stable surface film, while the surface film formed on BM specimen was unstable as time progressed, leading to a higher degree of corrosion. This was further corroborated with the results of weight loss measurements.
3. FSPed EZ33 alloy exhibited a relatively uniform in vivo corrosion behavior. The in vivo corrosion rate was maintained at an average of 1 mm/year until week eight and decreased to 0.7 mm/year until the termination of the study at week 12. Study of the control animal models suggested a bone recovery window of 8 weeks (Stage 3 of bone healing), which was similar to that observed for bone healing in pediatric patients. Osteoblastic activity was observed around the implant at four weeks leading to new bone formation around the implant at eight weeks. The FSPed EZ33 implant showed good osseointegration at eight weeks, stable corrosion rate, and did not create undesirable inflammation or produced toxic corrosion products.

Ethics approval and consent to participate

CRediT authorship contribution statement

Vasanth C. Shunmugasamy: Methodology, Investigation, Writing – original draft, Formal analysis, Writing – review & editing. **Marwa AbdelGawad:** Methodology, Investigation, Writing – original draft, Formal analysis, Writing – review & editing. **Muhammad Umar Sohail:** Methodology, Investigation, Writing – original draft, Formal analysis, Writing – review & editing. **Talal Ibrahim:** Methodology, Investigation, Supervision, Writing – review & editing. **Talha Khan:** Methodology, Investigation, Writing – review & editing. **Thomas Daniel Seers:** Methodology, Investigation, Writing – review & editing. **Bilal Mansoor:** Conceptualization, Methodology, Writing, Formal analysis, Writing – review & editing, Supervision, Project administration, Funding acquisition.

Declaration of competing interest

The authors declare that they have no known competing financial interests or personal relationships that could have appeared to influence the work reported in this paper.

Acknowledgement

References

[1] G. Reith, V. Schmitz-Greven, K.O. Hensel, M.M. Schneider, T. Tinschmann, B. Bouillon, C. Probst, Metal implant removal: benefits and drawbacks – a patient survey, BMC Surg. 15 (2015) 96, https://doi.org/10.1186/s12893-015-0081-6.

[2] R.B. Minkowitz, S. Bhadsavle, M. Walsh, K.A. Egol, Removal of painful orthopaedic implants after fracture union, J. Bone Jt. Surg. 89 (2007) 1906–1912.

[3] Q. Chen, G.A. Thouas, Metallic implant biomaterials, Mater. Sci. Eng. R Rep. 87 (2015) 1–57, https://doi.org/10.1016/j.mser.2014.10.001.

[4] M. Moravej, D. Mantovani, Biodegradable metals for cardiovascular stent application: interests and new opportunities, Int. J. Mol. Sci. 12 (2011) 4250–4270.

[5] S.F. Fischerauer, T. Kraus, X. Wu, S. Tangl, E. Sorantin, A.C. Hänzi, J.F. Löffler, P. J. Uggowitzer, A.M. Weinberg, In vivo degradation performance of micro-arc-oxidized magnesium implants: a micro-CT study in rats, Acta Biomater. 9 (2013) 5411–5420, https://doi.org/10.1016/j.actbio.2012.09.017.

[6] K.F. Farraro, K.E. Kim, S.L.-Y. Woo, J.R. Flowers, M.B. McCullough, Revolutionizing orthopaedic biomaterials: the potential of biodegradable and bioresorbable magnesium-based materials for functional tissue engineering, J. Biomech. 47 (2014) 1979–1986, https://doi.org/10.1016/j.jbiomech.2013.12.003.

[7] M.P. Staiger, A.M. Pietak, J. Huadmai, G. Dias, Magnesium and its alloys as orthopedic biomaterials: a review, Biomaterials 27 (2006) 1728–1734, https://doi.org/10.1016/j.biomaterials.2005.10.003.

[8] Y. Chen, Z. Xu, C. Smith, J. Sankar, Recent advances on the development of magnesium alloys for biodegradable implants, Acta Biomater. 10 (2014) 4561–4573, https://doi.org/10.1016/j.actbio.2014.07.005.

[9] D. Zhao, F. Witte, F. Lu, J. Wang, J. Li, L. Qin, Current status on clinical applications of magnesium-based orthopaedic implants: a review from clinical translational perspective, Biomaterials 112 (2017) 287–302, https://doi.org/10.1016/j.biomaterials.2016.10.017.

[10] Y. Yang, C. He, E. Dianyu, W. Yang, F. Qi, D. Xie, L. Shen, S. Peng, C. Shuai, Mg bone implant: features, developments and perspectives, Mater. Des. 185 (2020), 108259, https://doi.org/10.1016/j.matdes.2019.108259.

[11] F. Witte, The history of biodegradable magnesium implants: a review, Acta Biomater. 6 (2010) 1680–1692, https://doi.org/10.1016/j.actbio.2010.02.028.

[12] J. Espiritu, M. Meier, J.-M. Seitz, The current performance of biodegradable magnesium-based implants in magnetic resonance imaging: a review, Bioact. Mater. 6 (2021) 4360–4367, https://doi.org/10.1016/j.bioactmat.2021.04.012.

[13] E. Cerrato, U. Barbero, J.A. Gil Romero, G. Quadri, H. Mejia-Renteria, F. Tomassini, F. Ferrari, F. Varbella, N. Gonzalo, J. Escaned, Magmaris™ resorbable magnesium scaffold: state-of-art review, Fut. Cardiol. 15 (2019) 267–279, https://doi.org/10.2217/fca-2018-0081.

[14] X. Lin, Saijilafu, X. Wu, K. Wu, J. Chen, L. Tan, F. Witte, H. Yang, D. Mantovani, H. Zhou, C. Liang, Q. Yang, K. Yang, L. Yang, Biodegradable Mg-based alloys: biological implications and restorative opportunities, Int. Mater. Rev. (2022) 1–39, https://doi.org/10.1080/09506608.2022.2079367.

[15] T. Ren, X. Gao, C. Xu, L. Yang, P. Guo, H. Liu, Y. Chen, W. Sun, Z. Song, Evaluation of as-extruded ternary Zn–Mg–Zr alloys for biomedical implantation material: in vitro and in vivo behavior, Mater. Corros. 70 (2019) 1056–1070, https://doi.org/10.1002/maco.201810648.

[16] G.L. Song, A. Atrens, Corrosion mechanisms of magnesium alloys, Adv. Eng. Mater. 1 (1999) 11–33.

[17] M. Pourbaix, Atlas of electrochemical equilibria in aqueous solutions - translated from the French by JAMES A, in: FRANKLIN (Except Sections I, III 5 and III 6, Which Were Originally Written in English), second ed., 1974. Houston, TX.

[18] T.R. Thomaz, C.R. Weber, T. Pelegrini, L.F.P. Dick, G. Knörnschild, The negative difference effect of magnesium and of the AZ91 alloy in chloride and stannate-containing solutions, Corros. Sci. 52 (2010) 2235–2243, https://doi.org/10.1016/j.corsci.2010.03.010.

[19] S. Bender, J. Goellner, A. Heyn, S. Schmigalla, A new theory for the negative difference effect in magnesium corrosion, Mater. Corros. 63 (2012) 707–712, https://doi.org/10.1002/maco.201106225.

[20] S.S. Patil, R.D.K. Misra, M. Gao, Z. Ma, L. Tan, K. Yang, Bioactive coating on a new Mg-2Zn-0.5Nd alloy: modulation of degradation rate and cellular response, Mater. Technol. 34 (2019) 394–402, https://doi.org/10.1080/10667857.2019.1574956.

[21] Y. Yang, F. Yuan, C. Gao, P. Feng, L. Xue, S. He, C. Shuai, A combined strategy to enhance the properties of Zn by laser rapid solidification and laser alloying, J. Mech. Behav. Biomed. Mater. 82 (2018) 51–60, https://doi.org/10.1016/j.jmbbm.2018.03.018.

[22] C. Shuai, S. Li, S. Peng, P. Feng, Y. Lai, C. Gao, Biodegradable metallic bone implants, Mater. Chem. Front. 3 (2019) 544–562, https://doi.org/10.1039/C8QM00507A.

[23] M. Erinc, W.H. Sillekens, R.G.T.M. Mannens, R.J. Werkhoven, Applicability of existing magnesium alloys as biomedical implant materials, in: E.A. Nyberg, S.

[24] R. Agnew, N.R. Neelameggham, M.O. Pekguleiyw (Eds.), Magnes. Technol. 2009, TMS, The Minerals, Metals & Materials Society, 2009, pp. 209–214.

[24] R. Erbel, C. Di Mario, J. Bartunek, J. Bonnier, B. de Bruyne, F.R. Eberli, P. Erne, M. Haude, B. Heublein, M. Horrigan, C. Ilsley, D. Böse, J. Koolen, N. Lüscher, T. F. Weissman, R. Waksman, Temporary scaffolding of coronary arteries with bioabsorbable magnesium stents: a prospective, non-randomised multicentre trial, Lancet 369 (2007) 1869–1875.

[25] P.W. Serruys, M.J.B. Kutryk, A.T.L. Ong, Coronary-artery stents, N. Engl. J. Med. 354 (2006) 483–495, https://doi.org/10.1056/NEJMra051091.

[26] H. Hermawan, D. Dubé, D. Mantovani, Developments in metallic biodegradable stents, Acta Biomater. 6 (2010) 1693–1697, https://doi.org/10.1016/j.actbio.2009.10.006.

[27] C.A. Malone, N.J. Sauer, T.W. Fenton, A radiographic assessment of pediatric fracture healing and time since injury, J. Forensic Sci. 56 (2011) 1123–1130, https://doi.org/10.1111/j.1556-4029.2011.01820.x.

[28] X. Guan, M. Xiong, F. Zeng, B. Xu, L. Yang, H. Guo, J. Niu, J. Zhang, C. Chen, J. Pei, H. Huang, G. Yuan, Enhancement of osteogenesis and biodegradation control by brushite coating on Mg–Nd–Zn–Zr alloy for mandibular bone repair, ACS Appl. Mater. Interfaces 6 (2014) 21525–21533, https://doi.org/10.1021/am506543a.

[29] T. van den Bos, D. Speijer, R.A. Bank, D. Brömme, V. Everts, Differences in matrix composition between calvaria and long bone in mice suggest differences in biomechanical properties and resorption: special emphasis on collagen, Bone 43 (2008) 459–468.

[30] Y. Ding, C. Wen, P. Hodgson, Y. Li, Effects of alloying elements on the corrosion behavior and biocompatibility of biodegradable magnesium alloys: a review, J. Mater. Chem. B 2 (2014) 1912–1933, https://doi.org/10.1039/C3TB21746A.

[31] S. Tekumalla, S. Seetharaman, A. Almajid, M. Gupta, H.F. Lopez, Mechanical properties of magnesium-rare earth alloy systems: a review, Metals 5 (2015) 1–39, https://doi.org/10.3390/met5010001.

[32] D. Li, D. Zhang, Q. Yuan, L. Liu, H. Li, L. Xiong, X. Guo, Y. Yan, K. Yu, Y. Dai, T. Xiao, Y. Li, C. Wen, In vitro and in vivo assessment of the effect of biodegradable magnesium alloys on osteogenesis, Acta Biomater. 141 (2022) 454–465, https://doi.org/10.1016/j.actbio.2021.12.032.

[33] P. Trumbo, S. Schlicker, A.A. Yates, M. Poos, Dietary reference intakes for energy, carbohydrate, fiber, fat, fatty acids, cholesterol, protein and amino acids, J. Am. Diet Assoc. 102 (2002) 1621–1630, https://doi.org/10.1016/S0002-8223(02)90346-9.

[34] Y. Song, E.-H. Han, D. Shan, C.D. Yim, B.S. You, The effect of Zn concentration on the corrosion behavior of Mg–xZn alloys, Corros. Sci. 65 (2012) 322–330, https://doi.org/10.1016/j.corsci.2012.08.037.

[35] S. Cai, T. Lei, N. Li, F. Feng, Effects of Zn on microstructure, mechanical properties and corrosion behavior of Mg–Zn alloys, Mater. Sci. Eng. C 32 (2012) 2570–2577, https://doi.org/10.1016/j.msec.2012.07.042.

[36] E. Koç, M.B. Kannan, M. Ünal, E. Candan, Influence of zinc on the microstructure, mechanical properties and in vitro corrosion behavior of magnesium–zinc binary alloys, J. Alloys Compd. 648 (2015) 291–296, https://doi.org/10.1016/j.jallcom.2015.06.227.

[37] D.H. StJohn, M. Qian, M.A. Easton, P. Cao, Z. Hildebrand, Grain refinement of magnesium alloys, Metall. Mater. Trans. 36 (2005) 1669–1679, https://doi.org/10.1007/s11661-005-0030-6.

[38] Y.C. Lee, A.K. Dahle, D.H. StJohn, The role of solute in grain refinement of magnesium, Metall. Mater. Trans. 31 (2000) 2895–2906, https://doi.org/10.1007/BF02830349.

[39] T. Bhattacharjee, C.L. Mendis, T.T. Sasaki, T. Ohkubo, K. Hono, Effect of Zr addition on the precipitation in Mg–Zn-based alloy, Scr. Mater. 67 (2012) 967–970, https://doi.org/10.1016/j.scriptamat.2012.08.031.

[40] T. Bhattacharjee, T. Nakata, T.T. Sasaki, S. Kamado, K. Hono, Effect of microalloyed Zr on the extruded microstructure of Mg–6.2Zn-based alloys, Scr. Mater. 90–91 (2014) 37–40, https://doi.org/10.1016/j.scriptamat.2014.07.011.

[41] C. Rössig, N. Angrisani, P. Helmecke, S. Besdo, J.-M. Seitz, B. Welke, N. Fedchenko, H. Kock, J. Reifenrath, In vivo evaluation of a magnesium-based degradable intramedullary nailing system in a sheep model, Acta Biomater. 25 (2015) 369–383, https://doi.org/10.1016/j.actbio.2015.07.025.

[42] A. Myrissa, S. Braeuer, E. Martinelli, R. Willumeit-Römer, W. Goessler, A. M. Weinberg, Gadolinium accumulation in organs of Sprague–Dawley® rats after implantation of a biodegradable magnesium-gadolinium alloy, Acta Biomater. 48 (2017) 521–529, https://doi.org/10.1016/j.actbio.2016.11.024.

[43] E. Willbold, X. Gu, D. Albert, K. Kalla, K. Bobe, M. Brauneis, C. Janning, J. Nellesen, W. Czayka, W. Tillmann, Y. Zheng, F. Witte, Effect of the addition of low rare earth elements (lanthanum, neodymium, cerium) on the biodegradation and biocompatibility of magnesium, Acta Biomater. 11 (2015) 554–562, https://doi.org/10.1016/j.actbio.2014.09.041.

[44] F. Amerstorfer, S.F. Fischerauer, L. Fischer, J. Eichler, J. Draxler, A. Zitek, M. Meischel, E. Martinelli, T. Kraus, S. Hann, S.E. Stanzl-Tschegg, P. J. Uggowitzer, J.F. Löffler, A.M. Weinberg, T. Prohaska, Long-term in vivo degradation behavior and near-implant distribution of resorbed elements for magnesium alloys WZ21 and ZX50, Acta Biomater. 42 (2016) 440–450, https://doi.org/10.1016/j.actbio.2016.06.025.

[45] J. Zhang, H. Li, W. Wang, H. Huang, J. Pei, H. Qu, G. Yuan, Y. Li, The degradation and transport mechanism of a Mg-Nd-Zn-Zr stent in rabbit common carotid artery: a 20-month study, Acta Biomater. 69 (2018) 372–384, https://doi.org/10.1016/j.actbio.2018.01.018.

[46] M. AbdelGawad, B. Mansoor, A.U. Chaudhry, Corrosion characteristics of two rare earth containing magnesium alloys, in: D. Orlov, V. Joshi, K.N. Solanki, N.

R. Neelameggham (Eds.), Magnes. Technol. 2018, TMS - Miner. Met. Mater. Ser., Springer International Publishing, Cham, 2018, pp. 43–53.

[47] M. AbdelGawad, A.U. Chaudhry, B. Mansoor, The influence of temperature and medium on corrosion response of ZE41 and EZ33, in: V. V Joshi, J.B. Jordon, D. Orlov, N.R. Neelameggham (Eds.), Magnes. Technol. 2019, TMS - Miner. Met. Mater. Ser., Springer International Publishing, Cham, 2019, pp. 159–167.

[48] A. Marwa, C.A. Usman, V.C. Shunmugasamy, I. Karaman, B. Mansoor, Corrosion behavior of Mg-Zn-Zr-RE alloys under physiological environment – impact on mechanical integrity and biocompatibility, J. Magn. Alloys 10 (2022) 1542–1572.

[49] A.E. Coy, F. Viejo, P. Skeldon, G.E. Thompson, Susceptibility of rare-earth-magnesium alloys to micro-galvanic corrosion, Corros. Sci. 52 (2010) 3896–3906, https://doi.org/10.1016/j.corsci.2010.08.006.

[50] M. Kasaeian-Naeini, M. Sedighi, R. Hashemi, Severe plastic deformation (SPD) of biodegradable magnesium alloys and composites: a review of developments and prospects, J. Magn. Alloys 10 (2022) 938–955, https://doi.org/10.1016/j.jma.2021.11.006.

[51] R.S. Mishra, P.S. De, N. Kumar, Friction stir processing, in: R.S. Mishra, P.S. De, N. Kumar (Eds.), Frict. Stir Weld. Process. Sci. Eng., Springer International Publishing, Cham, 2014, pp. 259–296, https://doi.org/10.1007/978-3-319-07043-8_9.

[52] N. Birbilis, K.D. Ralston, S. Virtanen, H.L. Fraser, C.H.J. Davies, Grain character influences on corrosion of ECAPed pure magnesium, Corros. Eng. Sci. Technol. 45 (2010) 224–230, https://doi.org/10.1179/147842209X12559428167805.

[53] R.S. Mishra, Z.Y. Ma, Friction stir welding and processing, Mater. Sci. Eng. R Rep. 50 (2005) 1–78, https://doi.org/10.1016/j.mser.2005.07.001.

[54] G.R. Argade, S.K. Panigrahi, R.S. Mishra, Effects of grain size on the corrosion resistance of wrought magnesium alloys containing neodymium, Corros. Sci. 58 (2012) 145–151, https://doi.org/10.1016/j.corsci.2012.01.021.

[55] W. Zhang, L. Tan, D. Ni, J. Chen, Y.C. Zhao, L. Liu, C. Shuai, K. Yang, A. Atrens, M.C. Zhao, Effect of grain refinement and crystallographic texture produced by friction stir processing on the biodegradation behavior of a Mg-Nd-Zn alloy, J. Mater. Sci. Technol. 35 (2019) 777–783, https://doi.org/10.1016/j.jmst.2018.11.025.

[56] Y. Luo, Y. Deng, L. Guan, L. Ye, X. Guo, A. Luo, Effect of grain size and crystal orientation on the corrosion behavior of as-extruded Mg-6Gd-2Y-0.2Zr alloy, Corros. Sci. 164 (2020), 108338, https://doi.org/10.1016/j.corsci.2019.108338.

[57] S. Pawar, T.J.A. Slater, T.L. Burnett, X. Zhou, G.M. Scamans, Z. Fan, G. E. Thompson, P.J. Withers, Crystallographic effects on the corrosion of twin roll cast AZ31 Mg alloy sheet, Acta Mater. 133 (2017) 90–99, https://doi.org/10.1016/j.actamat.2017.05.027.

[58] A. Atrens, G.-L. Song, M. Liu, Z. Shi, F. Cao, M.S. Dargusch, Review of recent developments in the field of magnesium corrosion, Adv. Eng. Mater. 17 (2015) 400–453, https://doi.org/10.1002/adem.201400434.

[59] R. Xin, Y. Luo, A. Zuo, J. Gao, Q. Liu, Texture effect on corrosion behavior of AZ31 Mg alloy in simulated physiological environment, Mater. Lett. 72 (2012) 1–4, https://doi.org/10.1016/j.matlet.2011.11.032.

[60] K. Hagihara, M. Okubo, M. Yamasaki, T. Nakano, Crystal-orientation-dependent corrosion behaviour of single crystals of a pure Mg and Mg-Al and Mg-Cu solid solutions, Corros. Sci. 109 (2016) 68–85, https://doi.org/10.1016/j.corsci.2016.03.019.

[61] G.-L. Song, R. Mishra, Z. Xu, Crystallographic orientation and electrochemical activity of AZ31 Mg alloy, Electrochem. Commun. 12 (2010) 1009–1012, https://doi.org/10.1016/j.elecom.2010.05.011.

[62] S. Yin, W. Duan, W. Liu, L. Wu, J. Yu, Z. Zhao, M. Liu, P. Wang, J. Cui, Z. Zhang, Influence of specific second phases on corrosion behaviors of Mg-Zn-Gd-Zr alloys, Corros. Sci. 166 (2020), https://doi.org/10.1016/j.corsci.2019.108419.

[63] W. Yuan, R.S. Mishra, B. Carlson, R.K. Mishra, R. Verma, R. Kubic, Effect of texture on the mechanical behavior of ultrafine grained magnesium alloy, Scr. Mater. 64 (2011) 580–583, https://doi.org/10.1016/j.scriptamat.2010.11.052.

[64] W. Yuan, R.S. Mishra, B. Carlson, R. Verma, R.K. Mishra, Material flow and microstructural evolution during friction stir spot welding of AZ31 magnesium alloy, Mater. Sci. Eng. 543 (2012) 200–209, https://doi.org/10.1016/j.msea.2012.02.075.

[65] S.H.C. Park, Y.S. Sato, H. Kokawa, Basal plane texture and flow pattern in friction stir weld of a magnesium alloy, Metall. Mater. Trans. 34 (2003) 987–994, https://doi.org/10.1007/s11661-003-0228-4.

[66] B. Mansoor, A.K. Ghosh, Microstructure and tensile behavior of a friction stir processed magnesium alloy, Acta Mater. 60 (2012) 5079–5088.

[67] A. Raja, V. Pancholi, Effect of friction stir processing on tensile and fracture behaviour of AZ91 alloy, J. Mater. Process. Technol. 248 (2017) 8–17, https://doi.org/10.1016/j.jmatprotec.2017.05.001.

[68] N. Kumar, N. Dendge, R. Banerjee, R.S. Mishra, Effect of microstructure on the uniaxial tensile deformation behavior of Mg-4Y–3RE alloy, Mater. Sci. Eng. 590 (2014) 116–131, https://doi.org/10.1016/j.msea.2013.10.009.

[69] P.G. Partridge, The crystallography and deformation modes of hexagonal close-packed metals, Metall. Rev. 12 (1967) 169–194, https://doi.org/10.1179/mtlr.1967.12.1.169.

[70] T. Mukai, M. Yamanoi, H. Watanabe, K. Higashi, Ductility enhancement in AZ31 magnesium alloy by controlling its grain structure, Scr. Mater. 45 (2001) 89–94, https://doi.org/10.1016/S1359-6462(01)00996-4.

[71] A. Yamashita, Z. Horita, T.G. Langdon, Improving the mechanical properties of magnesium and a magnesium alloy through severe plastic deformation, Mater. Sci. Eng. 300 (2001) 142–147, https://doi.org/10.1016/S0921-5093(00)01660-9.

[72] A. Dorbane, B. Mansoor, G. Ayoub, V.C. Shunmugasamy, A. Imad, Mechanical, microstructural and fracture properties of dissimilar welds produced by friction stir welding of AZ31B and Al6061, Mater. Sci. Eng. 651 (2016) 720–733.

[73] NACE/ASTM G31 - 12a: Standard Guide for Laboratory Immersion Corrosion Testing of Metals, ASTM International, West Conshohocken, PA, 2012, https://doi.org/10.1520/NACEASTMG0031-12A (n.d.).

[74] ISO 10993-5:2009 Biological Evaluation of Medical Devices — Part 5: Tests for in Vitro Cytotoxicity, (n.d.).

[75] F. Witte, J. Fischer, J. Nellesen, C. Vogt, J. Vogt, T. Donath, F. Beckmann, In Vivo corrosion and corrosion protection of magnesium alloy LAE442, Acta Biomater. 6 (2010) 1792–1799, https://doi.org/10.1016/j.actbio.2009.10.012.

[76] A. Buades, B. Coll, J.-M. Morel, Non-local means denoising, Image Process. Line 1 (2011) 208–212.

[77] A.M. Gressner, T. Arndt, Encyclopedia of medical laboratory diagnostics, in: Volume 1: Clinical Chemistry, Springer-Verlag, Berlin, Germany, 2012.

[78] T. Ryspaev, Z. Trojanová, O. Padalka, V. Wesling, Microstructure of superplastic QE22 and EZ33 magnesium alloys, Mater. Lett. 62 (2008) 4041–4043, https://doi.org/10.1016/j.matlet.2008.05.063.

[79] L.Y. Wei, G.L. Dunlop, H. Westengen, The intergranular microstructure of cast Mg-Zn and Mg-Zn-rare earth alloys, Metall. Mater. Trans. 26 (1995) 1947–1955, https://doi.org/10.1007/BF02670666.

[80] L.Y. Wei, G.L. Dunlop, Crystal symmetry of the pseudo-ternary T-phases in Mg-Zn-rare earth alloys, J. Mater. Sci. Lett. 15 (1996) 4–7, https://doi.org/10.1007/BF01855594.

[81] Y.N. Wang, C.I. Chang, C.J. Lee, H.K. Lin, J.C. Huang, Texture and weak grain size dependence in friction stir processed Mg–Al–Zn alloy, Scr. Mater. 55 (2006) 637–640, https://doi.org/10.1016/j.scriptamat.2006.06.005.

[82] J. Peng, Z. Zhang, Z. Liu, Y. Li, P. Guo, W. Zhou, Y. Wu, The effect of texture and grain size on improving the mechanical properties of Mg-Al-Zn alloys by friction stir processing, Sci. Rep. 8 (2018) 4196, https://doi.org/10.1038/s41598-018-22344-3.

[83] Q. Liu, G. Chen, S. Zeng, S. Zhang, F. Long, Q. Shi, The corrosion behavior of Mg-9Al-xRE magnesium alloys modified by friction stir processing, J. Alloys Compd. 851 (2021), 156835, https://doi.org/10.1016/j.jallcom.2020.156835.

[84] G. Pagano, M. Guida, F. Tommasi, R. Oral, Health effects and toxicity mechanisms of rare earth elements-Knowledge gaps and research prospects, Ecotoxicol. Environ. Saf. 115 (2015) 40–48, https://doi.org/10.1016/j.ecoenv.2015.01.030.

[85] F. Feyerabend, J. Fischer, J. Holtz, F. Witte, R. Willumeit, H. Drücker, C. Vogt, N. Hort, Evaluation of short-term effects of rare earth and other elements used in magnesium alloys on primary cells and cell lines, Acta Biomater. 6 (2010) 1834–1842, https://doi.org/10.1016/j.actbio.2009.09.024.

[86] A. Benedetto, C. Bocca, P. Brizio, S. Cannito, M.C. Abete, S. Squadrone, Effects of the rare elements lanthanum and cerium on the growth of colorectal and hepatic cancer cell lines, Toxicol. Vitro 46 (2018) 9–18, https://doi.org/10.1016/j.tiv.2017.09.024.

[87] J. Li, M.A. Kacena, D.L. Stocum, Fracture healing, in: D.B. Burr, M. Allen (Eds.), Basic Appl. Bone Biol., Academic Press, 2019, pp. 235–253, https://doi.org/10.1016/B978-0-12-813259-3.00012-9.

[88] J. Devitt, Musculoskeletal healing process, in: M. Khodaee, A.L. Waterbrook, M. Gammons (Eds.), Sport. Fract. Dislocations Trauma, Springer International Publishing, Cham, 2020, pp. 97–104, https://doi.org/10.1007/978-3-030-36790-9_10.

[89] T. Kraus, S.F. Fischerauer, A.C. Hänzi, P.J. Uggowitzer, J.F. Löffler, A. M. Weinberg, Magnesium alloys for temporary implants in osteosynthesis: in vivo studies of their degradation and interaction with bone, Acta Biomater. 8 (2012) 1230–1238, https://doi.org/10.1016/j.actbio.2011.11.008.

[90] X.N. Gu, X.H. Xie, N. Li, Y.F. Zheng, L. Qin, In vitro and in vivo studies on a Mg–Sr binary alloy system developed as a new kind of biodegradable metal, Acta Biomater. 8 (2012) 2360–2374, https://doi.org/10.1016/j.actbio.2012.02.018.

[91] S. Zhang, X. Zhang, C. Zhao, J. Li, Y. Song, C. Xie, H. Tao, Y. Zhang, Y. He, Y. Jiang, Y. Bian, Research on an Mg–Zn alloy as a degradable biomaterial, Acta Biomater. 6 (2010) 626–640, https://doi.org/10.1016/j.actbio.2009.06.028.

[92] A.H.M. Sanchez, B.J.C. Luthringer, F. Feyerabend, R. Willumeit, Mg and Mg alloys: How comparable are in vitro and in vivo corrosion rates? A review, Acta Biomater. 13 (2015) 16–31, https://doi.org/10.1016/j.actbio.2014.11.048.

[93] C.I. Chang, X.H. Du, J.C. Huang, Achieving ultrafine grain size in Mg–Al–Zn alloy by friction stir processing, Scr. Mater. 57 (2007) 209–212, https://doi.org/10.1016/j.scriptamat.2007.04.007.

[94] H. Yu, Y. Xin, M. Wang, Q. Liu, Hall-Petch relationship in Mg alloys: a review, J. Mater. Sci. Technol. 34 (2018) 248–256, https://doi.org/10.1016/j.jmst.2017.07.022.

[95] M. Venkataiah, T. Anup Kumar, K. Venkata Rao, S. Anand Kumar, I. Siva, B. Ratna Sunil, Effect of grain refinement on corrosion rate, mechanical and machining behavior of friction stir processed ZE41 Mg alloy, Trans. Indian Inst. Met. 72 (2019) 123–132, https://doi.org/10.1007/s12666-018-1467-9.

[96] F.K. MD, G.M. Karthik, S.K. Panigrahi, G.D. Janaki Ram, Friction stir processing of QE22 magnesium alloy to achieve ultrafine-grained microstructure with enhanced room temperature ductility and texture weakening, Mater. Charact. 147 (2019) 365–378, https://doi.org/10.1016/j.matchar.2018.11.020.

[97] B. Darras, E. Kishta, Submerged friction stir processing of AZ31 Magnesium alloy, Mater. Des. 47 (2013) 133–137, https://doi.org/10.1016/j.matdes.2012.12.026.

[98] Y.S. Sato, S.H.C. Park, A. Matsunaga, A. Honda, H. Kokawa, Novel production for highly formable Mg alloy plate, J. Mater. Sci. 40 (2005) 637–642, https://doi.org/10.1007/s10853-005-6301-1.

[99] Y. Jin, K. Wang, W. Wang, P. Peng, S. Zhou, L. Huang, T. Yang, K. Qiao, B. Zhang, J. Cai, HailiangYu, Microstructure and mechanical properties of AE42 rare earth-

containing magnesium alloy prepared by friction stir processing, Mater. Charact. 150 (2019) 52–61, https://doi.org/10.1016/j.matchar.2019.02.008.

[100] W. Wang, P. Han, P. Peng, T. Zhang, Q. Liu, S.-N. Yuan, L.-Y. Huang, H.-L. Yu, K. Qiao, K.-S. Wang, Friction stir processing of magnesium alloys: a review, Acta Metall. Sin. 33 (2020) 43–57, https://doi.org/10.1007/s40195-019-00971-7.

[101] G. Wu, J.M. Ibrahim, P.K. Chu, Surface design of biodegradable magnesium alloys — a review, Surf. Coating Technol. 233 (2013) 2–12, https://doi.org/10.1016/j.surfcoat.2012.10.009.

[102] M.N. Sarian, N. Iqbal, P. Sotoudehbagha, M. Razavi, Q.U. Ahmed, C. Sukotjo, H. Hermawan, Potential bioactive coating system for high-performance absorbable magnesium bone implants, Bioact. Mater. 12 (2022) 42–63, https://doi.org/10.1016/j.bioactmat.2021.10.034.

[103] S. Julmi, A.-K. Krüger, A.-C. Waselau, A. Meyer-Lindenberg, P. Wriggers, C. Klose, H.J. Maier, Processing and coating of open-pored absorbable magnesium-based bone implants, Mater. Sci. Eng. C 98 (2019) 1073–1086, https://doi.org/10.1016/j.msec.2018.12.125.

[104] Z. Li, X. Gu, S. Lou, Y. Zheng, The development of binary Mg–Ca alloys for use as biodegradable materials within bone, Biomaterials 29 (2008) 1329–1344, https://doi.org/10.1016/j.biomaterials.2007.12.021.

[105] A.L. Boskey, Bone composition: relationship to bone fragility and antiosteoporotic drug effects, BoneKEy Rep. 2 (2013) 447, https://doi.org/10.1038/bonekey.2013.181.

[106] A. Sionkowska, J. Kozłowska, Characterization of collagen/hydroxyapatite composite sponges as a potential bone substitute, Int. J. Biol. Macromol. 47 (2010) 483–487, https://doi.org/10.1016/j.ijbiomac.2010.07.002.

[107] M.M. Stevens, Biomaterials for bone tissue engineering, Mater. Today 11 (2008) 18–25, https://doi.org/10.1016/S1369-7021(08)70086-5.

[108] F. Witte, V. Kaese, H. Haferkamp, E. Switzer, A. Meyer-Lindenberg, C.J. Wirth, H. Windhagen, In vivo corrosion of four magnesium alloys and the associated bone response, Biomaterials 26 (2005) 3557–3563, https://doi.org/10.1016/j.biomaterials.2004.09.049.